#### **ORIGINAL PAPER**



# An Integrated Approach for Evaluation of Linear Cohesive Zone Model's Performance in Fracturing of Rocks

Prasoon Garg<sup>1</sup> • Bhardwaj Pandit<sup>2</sup> • Ahmadreza Hedayat<sup>1</sup> • D. V. Griffiths<sup>1</sup> • Gandluri Lakshminarasimha Sivakumar Babu<sup>2</sup>

Received: 3 January 2021 / Accepted: 22 June 2021 / Published online: 2 July 2021 © The Author(s), under exclusive licence to Springer-Verlag GmbH Austria, part of Springer Nature 2021

#### **Abstract**

Fracturing in rocks results in the formation of an inelastic region surrounding the crack tip called the fracture process zone (FPZ), which is often characterized using the Linear Cohesive Zone Model (LCZM). Various numerical studies have shown that the prediction of the FPZ characteristics is significantly influenced by variability in the input parameters of LCZM, such as crack tip opening displacement and tensile strength. In this study, an integrated approach was used for evaluating the LCZM performance in predicting fracture processes of Barre granite specimens, as a representative rock, under Mode I loading. The approach involved experimental testing, numerical simulation, uncertainty quantification of overall fracture behavior, and global sensitivity analysis. First, parameters of the LCZM were estimated from three-point bending tests on center notch Barre granite specimen using the two-dimensional digital image correlation (2D-DIC) technique. This was followed by the implementation of the LCZM in XFEM-based numerical model to simulate the evolution of the FPZ in tested geometry. The results from the deterministic numerical simulation showed that while LCZM can predict all stages of FPZ evolution, the variability in the experimental results, such as the FPZ size, cannot be accounted. The variability of the material response was quantified using a random variable analysis, which involved treating the LCZM's parameters as random variables. This was followed by the global sensitivity analysis that revealed the most sensitive input parameters is the tensile strength for accurate prediction of the global response of rock specimens under Mode I loading.

**Keywords** Fracture process zone (FPZ) · Digital image correlation (DIC) · Mode I fracture · Linear Cohesive Zone model (LCZM) · Response surface · Global sensitivity analysis (GSA)

<b>Abbreviations</b>		PDF	Probability distribution function
DIC	Digital image correlation	CMOD	Crack mouth opening displacement
CZM	Cohesive Zone model	H	Specimen height
LCZM	Linear Cohesive Zone model	B	Specimen thickness
FPZ	Fracture process zone	$a_0$	Notch length
FPZ-I	Fracture process zone initiation	CTOD	Crack tip opening displacement
TFZ	Traction free zone	x, y	Coordinates
RBF	Radial basis function	U	Displacement in x direction
MCS	Monte Carlo simulation	δ	Load-point displacement
GSA	Global sensitivity analysis	$\delta_{ m peak}$	Load-point displacement at peak load
NSE	Nash-Sutcliffe efficiency	$\delta_{ m norm}$	Normalized load-point displacement
COV	Coefficient of variation	$P_{\rm peak}$	Peak load
		$P_{\text{norm}}$	Normalized applied load
		w	Crack opening displacement
pgarg@mymail.mines.edu		$w_{\rm e}$	Elastic opening displacement
1		$w_{\rm ne}$	Inelastic crack opening displacement
Department of Civil and Environmental Engineering, Colorado School of Mines, Golden, CO 80401, USA		$w_{\rm c}$	Critical crack opening displacement
		$w_{\rm ne}^{\rm c}$	Critical inelastic crack opening
Department of Civil Engineering, Indian Institute of Science, Bangalore, India			displacement



Developing and fully developed frac-
ture process zone
Cohesive stress
External tensile stress
Tensile strength of rock
Cohesive strength
Maximum principal stress
CTOD derivative
Mode I fracture energy based on CZM
Mode I fracture energy based on
LEFM
First order Sobol' index for ith input
parameter
Effects Sobol' index for ith input
parameter
Total displacement
Continuous and discontinuous part of
displacement
Heaviside enrichment function
Crack tip enrichment functions
Degrees of freedoms of the enriched
nodes
Standard nodal shape functions
Nodal displacement for standard nodes

Nodal subsets containing crack

## 1 Introduction

 $K_{\Gamma}, K_{\Lambda}$ 

The rock behavior is typically governed by the various fracturing processes such as initiation of new cracks and their interaction and not by the intact matrix as these processes often act as precursors of ultimate failure. The fracturing in rocks and other quasi-brittle such as concrete is often characterized by a significant size of an inelastic region surrounding the crack tips (Hoagland et al. 1973; Labuz et al. 1987). The inelastic deformation occurs due to the formation of a micro-cracking zone, also known as the fracture process zone (FPZ), which has a significant impact on the overall failure of laboratory-scale rock specimens, as its size is often comparable to pre-existing cracks (Backers et al. 2005; Ghamgosar and Erarslan 2016; Parisio et al. 2019). In recent years, various studies (Wang and Hu 2017; Zhang et al. 2018a, b; Yu et al. 2018; Lin et al. 2019a, b, 2020; Yang et al. 2019) have used the cohesive zone model (CZM) to characterize the formation of the FPZ in rocks. The CZM lumps the FPZ into a thin interface with a softening response in the form of traction (cohesive stresses inside FPZ)-separation (crack opening displacement (w)) law (Hillerborg et al. 1976; Planas et al. 2003). Despite its extensive application in characterizing the FPZ based on laboratory experiments, its implementation in simulating rock fracture has been limited to a few geometries of Mode I loading such as three-point bending test, disk-shaped compact tension test, short-rod fracture test, etc. (Fakhimi and Tarokh 2013; Khoramishad et al. 2013; Rinehart et al. 2015; Yang et al. 2019).

In this study, the Linear Cohesive Zone Model (LCZM) was used to simulate the FPZ evolution. This study's main objective was to assess the LCZM's capability in predicting various fracturing characteristics, such as the evolution of the FPZ and its size, along with the global response of the material. To achieve the main objective, fracturing in notched Barre granite specimens under *Mode* I loading was explored through an integrated approach involving experimental testing, numerical simulation, uncertainty quantification, and global sensitivity analysis.

Over the years, the CZM based on different softening law such as linear, bilinear, and exponential law has been used to predict the fracture behavior in different materials such as concrete, polymers based composites, and asphalt mixtures (Bazant and Planas 1997; Elices et al. 2002; Soares et al. 2003; Roesler et al. 2007; Song et al. 2006). The identification of suitable softening law plays an important role in the prediction of fracture behavior (Shet and Chandra 2004; De Borst 2003), which is typically done using various indirect methods that require inverse analysis (Elices et al. 2002; Oh and Kim 2013; Chen et al. 2014; Xu et al. 2014; Lin et al. 2020). These inverse analysis-based methods mostly rely on matching the global response of the specimens and thus can provide non-unique softening law (Bažant and Yu 2011). Alternatively, non-destructive optical techniques such as acoustic emission (Zhang et al. 2018a, b), speckle interferometry (Lin et al. 2009), and digital image correlation (DIC) (Le et al. 2014) have been increasingly used to characterize the CZM for rocks due to their ability to provide the fundamental information about different fracture characteristics inside the FPZ. Various studies (Ji et al. 2016; Zhang et al. 2018a, b) using DIC have characterized the evolution of the FPZ in three stages, namely: (1) elastic phase, (2) formation and propagation of the FPZ, and (3) macro-crack initiation. However, there is no consistent method to pinpoint the transition between these three stages. For instance, most studies (Le et al. 2014; Ji et al. 2016; Lu et al. 2019; Miao et al. 2020) characterized the tip of the FPZ, i.e., the boundary between the elastic zone and the FPZ, as a merged position of displacement contour without any support from existing fracture model (Lin et al. 2020). As a result, a considerable variation in parameters of CZM is found for rocks as seen in Berea sandstone (Lin and Labuz 2013; Lin et al. 2019b), with significant scatter in the critical opening displacement (30–100 μm) and fracture energy (75–140 J/m<sup>2</sup>). Additionally, these fracture properties, due to their localized nature, are strongly influenced by material inhomogeneity and grain size, and thus, are difficult to estimate (Lin et al. 2019a).

Numerical simulations can provide valuable insights into the kinematic of the FPZ during fracture propagation



compared to laboratory experiments. However, due to the uncertainty in parameters of the CZM, few applications can be found in rocks (Yao 2012; Fakhimi and Tarokh 2013; Khoramishad et al. 2013; Rinehart et al. 2015; Xie et al. 2017; Yang et al. 2019). For instance, Rinehart et al. (2015), based on the implementation of the LCZM in Limestone specimens, found that accurate estimation of material properties is vital for the proper prediction of fracture processes and the global response of the rock specimens. The accuracy of prediction from the CZM is further complicated by material heterogeneity in rocks, which is responsible for a large variation in its fracture properties such as tensile strength  $(\sigma_t)$  and fracture toughness (Aliha and Ayatollahi 2014; Aliha et al. 2018). Besides material heterogeneity, uncertainties can also occur due to other sources such as the natural variation of properties, imperfections, and unpredictability caused by the lack of sufficient information on parameters or models (Baecher and Christian 2003). Therefore, it is vital to quantify the extent of variability in fracture properties for proper characterization of the fracture behavior. The recent studies by Aliha et al. (2012), Aliha and Ayatollahi (2014) and Aliha et al. (2018) tried to achieve this by implementing statistical analyses that involved estimation of the probability of fracture using a larger number of test data (~15 samples) of various rocks such as Harsin marble and Guiting Limestone. However, these studies were based on LEFM (assuming the elastic stress distribution around crack tip) and, thus, did not account for the FPZ and its influence on overall fracture behavior. To characterize uncertainty in the CZM, variability in its input parameters is identified by testing a large number of specimens (Bažant and Yu 2011; Khoramishad et al. 2013; Rinehart et al. 2015). Alternatively, based on a range of limited data (4–5 tests), uncertainty in input parameters of the CZM is quantified and subsequently treated as random variables, which then can be used in a numerical model to provide a quantification of uncertainty in fracture characteristics such as the FPZ initiation and its size. Additionally, it is also essential to study the contribution of the variability of input parameters towards the variability in overall fracture behavior. This can be accomplished by conducting global sensitivity analysis (GSA) and ranking the input parameters according to their relative contribution. Two global sensitivity measures are widely used in the literature, namely: (a) variance-based (Sobol 1993) and (b) moment-independent sensitivity measures (Borgonovo 2007). Variance-based sensitivity measure is most often adopted due to its ability to provide a good understanding of the model structure (Oakley and O'Hagan 2004). Sobol indices quantify the relative percentage contribution of each input parameter in the total variance of the output. This is achieved by estimating the first-order effects (i.e., the percentage contribution of the individual variable alone) and total effects (i.e., first order in addition to the contribution caused by its interaction with other parameters). Literature involving the application of these methods to study the sensitivity of input parameters on rock engineering problems are sparse. Pandit et al. (2019) estimated global sensitivity measure-Sobol indices for rock mass parameters defined by the Hoek–Brown constitutive model for the jointed rock slope.

The objective of this study was to assess the ability of CZM to predict the overall fracture behavior of Barre granite rock using an integrated approach involving the four major steps, namely: (a) experimental analysis, (b) numerical simulation, (c) uncertainty quantification of fracture behavior, and (d) identification of most influence input parameters of the CZM. The previous study by authors (for details, see Garg et al. 2020) found that the LCZM (based on linear softening law) is suitable for characterizing the non-linear deformation inside FPZ of Barre granite specimen under Mode I loading. Additionally, various experimental studies have also found the LCZM to be a reasonable approximation of material behavior inside FPZ for various rocks (Yang et al. 2019; Xie et al. 2017; Zhang et al. 2018a, b; Xing et al. 2019; Lin et al. 2019a, b). A series of three-point bending tests were performed on center-notch Barre granite specimen to estimate parameters of LCZM, which was then implemented in XFEM-based numerical model. The uncertainty in the fracture behavior in terms of the peak load and the FPZ characteristics were then quantified by treating the fracture properties as random variables and conducting Monte Carlo simulation (MCS) on surrogate augmented radial basis function (RBF) based response surface of the numerical model. This is followed by a variance-based global sensitivity analysis for the identification of the most influential input parameters.

## 2 Experimental Design

## 2.1 Material and Testing Procedure

This study characterizes the fracture processes in Barre granite specimens. Barre granite is among the most extensively studied rocks, typically formed in the Devonian New Hampshire pluton series of Burlington, Vermont (USA) (Goldsmith et al. 1976; Dai and Xia 2010; Morgan et al. 2013; Moradian et al. 2016; Saadat and Taheri 2019). It has a consistent mineral composition with feldspar (65% by volume), quartz (25% by volume), and biotite (9% by volume) as its primary constituents (Iqbal and Mohanty 2006; Nasseri et al. 2010). It is a fine- to medium-grained granodiorite with an average grain size of 0.87 mm (Shirole et al. 2020). Due to its crystalline nature, the Barre granite rock has a porosity of 0.6% and a density of 2.59 g/cm³ (Iqbal and Mohanty 2006).



A large block of Barre granite was used to prepare prismatic specimens with dimensions of length  $L\!=\!150$  mm, height  $H\!=\!75$  mm, and thickness  $B\!=\!25$  mm (Fig. 1a). All the surfaces of each specimen were then grounded to ensure the desired level of dimension with the tolerance of  $\pm 0.20$  mm and smoothness with the tolerance of  $\Delta/d$  of 0.0043 mm in accordance with the ASTM D4543. The specimen thickness 'B' was kept small (25 mm) such that the specimen deforms under the plane stress condition, ensuring planar fracture across its entire thickness. In each sample, a center notch was created by the Colorado WaterJet Company with the aperture of 1.02 mm and 1.12 mm at its front and back end, respectively. The length of the notch,  $a_0$  is 26 mm (Fig. 1a).

The three-point bending tests were performed on the center-notched Barre granite specimens (specimens presented as BG-1, BG-2, BG-3, BG-4) using a servo-controlled MTS load frame with 50 kN capacity and measurement accuracy of 0.01 kN. The specimens were loaded by pushing the top cylinder at a constant vertical displacement (load-point displacement ( $\delta$ ) at the mid-span) rate of 0.2  $\mu$ m/s (Fig. 1a–c). Additionally, an extensometer called

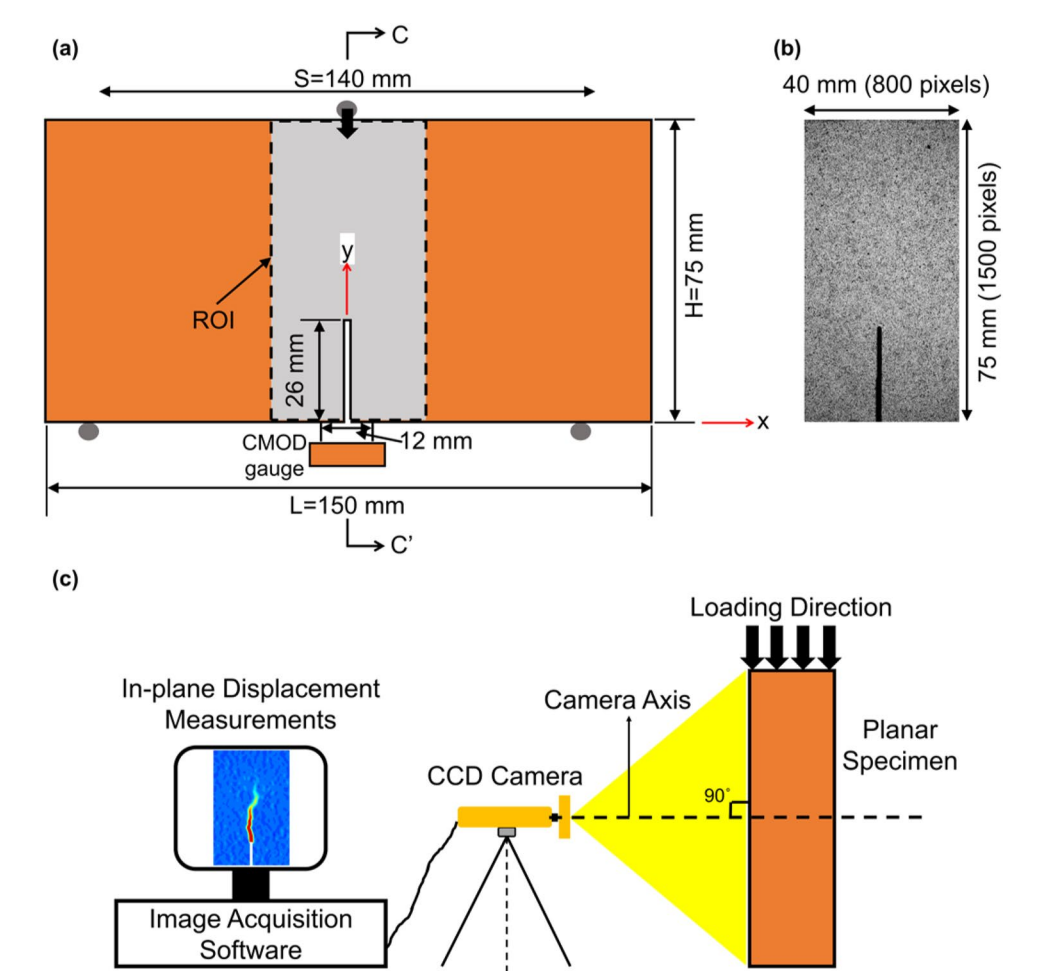
a clip-on gauge with a resolution of 1  $\mu$ m was bonded to the bottom surface of the beam to measure the crack mouth opening displacement (CMOD) (Fig. 1a). The CMOD represents the elongation of the bottom fiber of the beam and is measured as the displacement between two clips of extensometer across the gauge length of 12 mm. The relationships between Load–CMOD and Load–load-point displacement ( $\delta$ ) were recorded at a sampling rate of 12 points per second during the entire test run.

## 2.2 2D-Digital Image Correlation (2D-DIC) Setup

2D-DIC is one of the widely used non-contact optical methods for accurate estimation of the full-field surface deformation on geomaterials (Alam et al. 2014, 2015; Patel and Martin 2018; Garg et al. 2019; Miao et al. 2020). In 2D-DIC, unique speckles are tracked between two digital images of a planar surface (Pan et al. 2009a) in the undeformed (or reference) and deformed states. First, a region of interest (ROI) is defined in the reference image, which is divided into square grids with spacing equal to "step size." The motion of each grid point is assessed by tracking the neighboring group of

Section C-C'

Fig. 1 a Loading geometry of the three-point bending test along with the field of view for DIC analysis, b Image of the speckle pattern obtained on specimen BG-1, and c The schematic of the experimental setup used for a three-point test for synchronously capturing the crack propagation using the 2D-DIC. Figure not to scale





pixels called subsets (with a corresponding "subset size") between the current and the reference image. The subset is chosen rather than a single point because it contains a broader variation of gray-scale intensity values that can be uniquely identified in the deformed images (Bourcier et al. 2013). A statistical correlation criterion is used to track each subset (initially defined in reference images) in deformed images based on the assumption that gray-scale intensity values within subsets are preserved during specimen deformation (Schreier et al. 2009). Two types of correlation criteria, namely zero normalized cross-correlation (ZNCCD) and zero normalized sum of squared difference (ZNSSD), are commonly used for image correlation in DIC (Pan et al. 2009b). The algorithm implemented in these criteria defines a correlation coefficient to evaluate a degree of similarity between the reference and deformed subsets. The new position or displacement of the deformed subset is located by finding the extremum (minimum or maximum) position of the distribution of the correlation coefficient (Bourcier et al. 2013; Hedayat and Walton 2017). The displacement computed from the correlation procedure is then assigned to the center of the subset. The same procedure is then repeated for all grid points in the ROI to obtain the full-field displacement along the surface of the specimen at various stages of deformations (Hedayat et al. 2014). The strain field is computed by numerical differentiation of the full-field displacements, which are first smoothed within a local window (size defined by the "filter size") to minimize errors contained in estimated raw displacements and ensure reliable strain measurements. In this study, strain fields were calculated based on the Lagrangian approach of continuum mechanics (Dual and Schwarz 2012).

The proper implementation of the 2D-DIC method requires three steps: (a) specimen surface preparation, (b) experimental setup and image acquisition, and (c) the image correlation. The first step involves creating a stochastic pattern of gray-scale intensity values (speckle pattern) over the specimen surface. A high-quality speckle pattern typically has well-distributed gray-scale intensity values to ensure proper image correlation with low background noise (Sharpe 2008), which was achieved by spray painting the specimen surface using a combination of white and black paints (Fig. 1b). The applied speckle size ranged between 200 and 300 µm with each speckle containing 4–6 pixels as an isotropic magnification factor of  $M = 50 \mu m/pixel$  was used (Fig. 1b). This conforms to the recommendation of at least 3 pixels per speckle needed for proper image sampling during the image correlation process (Sutton et al. 2007).

In this study, a CCD camera with 2448 by 2048 square pixels capability was used in combination with a Fujinon lens of 17.5 mm focal length (Model CF35HA-1). The Pylon Viewer software was used to control the camera, which captured images of ROI of a small area of  $40 \times 75 \text{ mm}^2$  around

the center notch (Fig. 1b). During each three-point bending test, digital images of the speckled surface were captured at the rate of 12 frames/s until the total failure of the specimen. The images obtained were analyzed using the Correlated Solutions software (VIC-2D) to obtain surface deformation and strain field inside the ROI of each specimen.

A proper characterization of localized strain inside the FPZ typically depends on various DIC parameters such as subset size, step size, and filter size, which are entered as inputs in the VIC-2D software. In the current study, the subset size of 31 pixels is used as it is able to capture high strain values inside the FPZ without distorting its width (see details in Garg et al. (2020)). For similar reasons, the step size of 5 pixels and a filter size of 5 points was used in the current study, which ensures that the small width of the FPZ is accurately captured (see details in Garg et al. (2020)).

## 3 XFEM-Based Numerical Modeling

Since its inception, XFEM has been widely used in various fracture mechanics problems due to its effectiveness in modeling discontinuities in various static and dynamic crack problems (Elguedj et al. 2009; Khoei and Mohammadnejad 2011; Fan and Jing 2013; Sharafisafa and Nazem 2014; Zhuang et al. 2014; Eftekhari et al. 2015; Zhou et al. 2020). In the conventional FEM, modeling discontinuities such as cracks requires conformity of the mesh to the geometric discontinuities (Khoei 2014). Additionally, cracks in conventional FEM can only propagate along element edges and, thus, require remeshing with the formation of new cracks (Sharafisafa and Nazem 2014). The XFEM alleviates these problems using the partition of unity method, which allows elements that are intersected by discontinuities to be locally enriched while retaining properties of the stiffness matrix of the standard FEM (Moës and Belytschko 2002). In XFEM, cracks or voids are represented independent of the FE mesh by adding enrichment functions and additional degrees of freedom to the elements intersected by the crack (Karihaloo and Xiao 2003). The important concepts of XFEM along with the details of the implementation in the commercial software ABAQUS, are presented in this section.

#### 3.1 XFEM Representation of Cracks in ABAQUS

In XFEM formulation, displacement field (*u*) is approximated as a combination of continuous part and discontinuous part as given by (Belytschko and Black 1999; Zi and Belytschko 2003):

$$u(x) = u_{\text{cont}}(x) + u_{\text{disc}}(x), \tag{1}$$



where x represents position vector,  $u_{\rm cont}(x)$  is continuous displacement field and  $u_{\rm disc}(x)$  represents the discontinuous displacement field, which incorporates local enrichment functions to account for the presence of a crack. The displacement field in Eq. 1 can be rewritten as:

$$u(x) = \sum_{I} N_{I}(x)u_{I} + \sum_{I \in K_{\Gamma}} N_{I}(x)H(x)a_{J} + \sum_{I \in K_{\Lambda}} \left[ N_{I}(x) \sum_{\alpha=1}^{4} F_{\alpha}(x)b_{I\alpha} \right],$$
(2)

where  $N_I(x)$  represents standard shape functions and  $u_I$ represents the nodal displacement contribution due to the continuous part of the standard finite element solution. The H(x) is the Heaviside enrichment function that accounts for displacement jump across crack interior faces and  $F_{\alpha}(x)$ represent the crack tip enrichment functions that account for the elastic asymptotic fields near the crack tip (Giner et al. 2009).  $a_I$  and  $b_{I\alpha}$  are the degrees of freedoms (DOFs) vectors of the enriched nodes. The displacement contribution of the continuous part, i.e., first term at the right-hand side of Eq. 2, is estimated for all the nodes in the model domain.  $K_{\Gamma}$  and  $K_{\Lambda}$  belongs to the nodal subsets containing crack interior (shown by red circles in Fig. 2) and the crack tip (shown by yellow rectangles in Fig. 2). In XFEM, each node is only enriched with a single type of enrichment function and additional DOFs. For the 2D problems, nodes enriched with the Heaviside function have two additional DOFs, while nodes with crack tip enrichment functions have eight additional DOFs.

## 3.2 Crack Initiation and Propagation Criteria

In this study, the CZM was used to simulate the inelastic behavior of the material inside the FPZ. The CZM

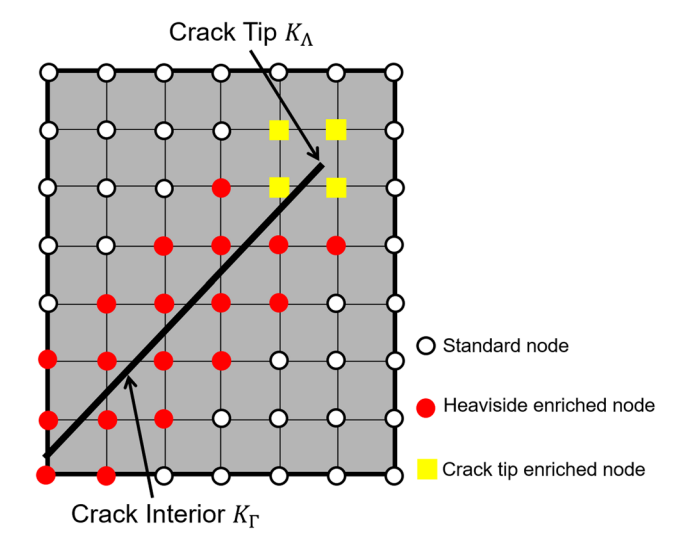


Fig. 2 Enriched elements in XFEM (after Xie et al. 2017)



(Hillerborg et al. 1976) lumps the FPZ ahead of the crack tip into a thin interface (also known as cohesive zone) that can transmit stresses across its faces (Fig. 3a). The nonlinear deformation inside the FPZ is represented by a constitutive relationship between cohesive stresses (traction between interface faces) and displacement jump across the thin interface (virtual crack plane). In pure Mode I fracture, the cohesive zone transmits the normal stress as a function of the crack opening displacement (w) (Fig. 3c). In the current study, LCZM was used as it is considered a reasonable constitutive response for characterizing the FPZ in most rocks (Reinhart et al. 2015; Xie et al. 2017; Zhang et al. 2018a, b; Xing et al. 2019; Yang et al. 2019; Lin et al. 2020). The LCZM assumes the material behavior to be linearly elastic from  $\sigma_n = 0$  to  $\sigma_n = \sigma_{n,\text{max}}$  (cohesive strength) with the associated limit of elastic opening displacement  $(w_e)$  Mode I fracture (Fig. 3c). At this stage, the FPZ initiates at the crack tip, which subsequently undergoes softening with the further increase in the crack opening displacement (w) and thus results in the degradation of the material's elastic stiffness (highlighted by light gray in Fig. 3c). The softening of the cohesive zone is characterized by a linear decrease in cohesive stress from  $\sigma_n = \sigma_{n,\text{max}}$ . with opening displacement at the elastic limit  $(w_e)$  to a critical opening displacement  $(w_c)$  where the cohesive stress reaches zero  $(\sigma_n = 0)$ . This implies that the material has undergone complete failure, resulting in the formation of a macro-crack (traction-free crack). The softening curve provides information about the energy dissipated inside the FPZ. The area under the softening curve is typically defined as the critical value of energy dissipation also known as fracture energy  $(G_F)$  (Bazant and Plaňas 1997; Zhang et al. 2018a, b; Lin et al. 2019b). The fracture energy  $(G_F)$  obtained from LCZM is equivalent to the critical energy release rate  $(G_{Ic})$  when the assumption of LEFM is valid (Lin et al. 2019b). For Mode I fracture, the constitutive relationship between cohesive stresses  $(\sigma_n(w))$ and crack opening displacement (w) is given by:

$$\begin{cases} \sigma_{n}(w) = \sigma_{n,\max}\left(\frac{w}{w_{e}}\right) & \left(0 \le w \le w_{e}\right) \\ \sigma_{n}(w) = \sigma_{n,\max}\left(1 - \frac{\left(w - w_{e}\right)}{\left(w_{e} - w_{e}\right)}\right) = \sigma_{n,\max}\left(1 - \frac{\left(w_{ne}\right)}{\left(w_{ne}^{e}\right)}\right) & \left(w_{e} \le w \le w_{e}\right) \end{cases} \end{cases}$$

$$(3a)$$

$$w_{\rm ne} = w - w_{\rm e}; \quad w_{\rm ne}^{\rm c} = w_{\rm c} - w_{\rm e},$$
 (3b)

where  $w_{\rm ne}$  is critical inelastic crack opening displacement and  $w_{\rm ne}^{\rm c}$  is the critical inelastic crack opening displacement. Both the elastic opening  $(w_{\rm e})$  and critical opening displacements  $(w_{\rm c})$  along with the size of the fully developed fracture process zone (L) are considered material properties. Therefore, the critical inelastic crack opening displacement  $(w_{\rm ne}^{\rm c})$  can also be considered as material property. The fracture

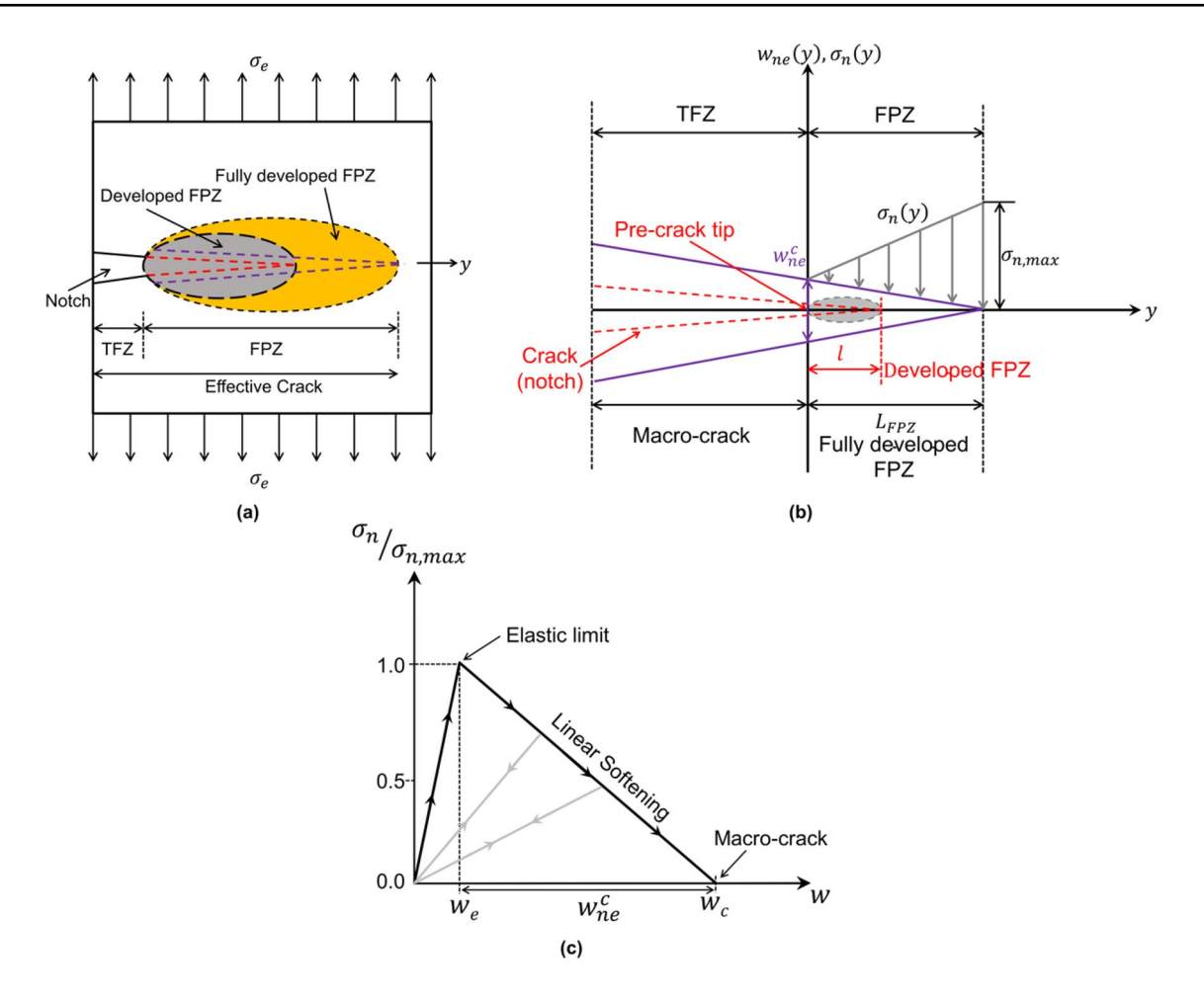


Fig. 3 a FPZ development in rocks, Linear cohesive zone model (LCZM) (b) with linear distribution of traction along the FPZ, and c linear softening law, traction-free zone (TFZ) (after Zhang et al. 2018a, b)

energy  $(G_F)$  (area under the softening curve) can be written as:

$$G_{\rm F} = \frac{1}{2} (\sigma_{n,\text{max}}) w_{\text{ne}}^{\text{c}}. \tag{4}$$

Therefore, LCZM characterize FPZ as a cohesive zone having a linear distribution of the normal stresses along its length with its maximum value ( $\sigma_n = \sigma_{n,\text{max}}$ ) at the tip of FPZ as shown in Fig. 3b.

In ABAQUS, the elastic response of the traction–separation law of the LCZM (Fig. 3c) is implemented based on the tensile elastic modulus ( $E_t$ ) of the material instead of using the elastic opening displacement ( $w_e$ ) (ABAQUS 2016). The FPZ initiation stage is then predicted using the Maximum Principal Stress (MPS) criterion as given by:

$$F = \left\{ \frac{\langle \sigma_{\text{max}} \rangle}{\sigma_{n,\text{max}}} \right\} = 1, \tag{5}$$

where  $\langle \sigma_{\text{max}} \rangle$  is maximum principal stress,  $\langle . \rangle$  represents the tensile component of stress, i.e.,  $\langle \sigma_{\text{max}} \rangle$  is equal to 0 when stresses are under pure compression ( $\sigma_{\text{max}} \leq 0$ ). The tensile stress is considered to be positive in the current study. Therefore, at the FPZ initiation stage, the maximum principal stress  $\langle \sigma_{\rm max} \rangle$  in an element exceeds cohesive strength of the material ( $\sigma_{n,\text{max}}$ ). The cohesive strength  $\sigma_{n,\text{max}}$  is typically assumed equal to the indirect tensile strength ( $\sigma_t$ ) of the material, estimated from Brazilian tests (Bazant and Planas 1997; Song et al. 2006). After the FPZ initiation, the softening is implemented by decreasing the cohesive stresses as a function of the inelastic crack opening displacement  $(w_{ne})$  as shown in Eq. 4. In the present study, various parameters of the LCZM such as critical inelastic crack opening  $(w_{ne}^{c})$  and the size of the fully developed fracture process zone  $(L_{\text{FPZ}})$ were estimated using the displacement approach of 2D-DIC.



mesh is used in the vicinity of the notch tip. To simulate

actual laboratory testing conditions, physical rollers were modeled with bottom rollers being fixed in both x and y

directions, and the top roller being fixed in the x-direction

(Fig. 4). Each physical roller was simulated as a rigid cyl-

inder and had frictionless contact with the specimen. The specimen was loaded by assigning the vertical displace-

ment on the top roller at a rate of 0.1 mm/step. As a result,

the analysis ended when the vertical displacement of the

top roller reached 0.1 mm. The applied load on the beam

was estimated based on the reaction force on the top roller. Additionally, similar to laboratory tests, the crack (notch)

mouth opening displacement (CMOD) also was recorded

at the gage length of 12 mm in the numerical model. The ABAQUS/standard was used to perform the numerical sim-

ulation, which implemented implicit static stress analyses

based on Newton–Raphson method with automatic incremental loading (ABAQUS 2016). The implicit analysis with

automatic incremental loading primarily focuses on ensur-

ing numerical stability during the entire loading stage; as

a result, no influence of loading rate was found. The entire

specimen was divided into three partitions to achieve a finer

mesh in the area around the notch tip with a lower computational time (Fig. 4). The model was discretized using

a 4-node bilinear plane stress quadrilateral elements with

a mean size of 0.2 mm in the central partition, while the remaining area had a coarser mesh with a mean size of

2 mm (Fig. 4). The elements size of 0.2 mm in the central partition of the beam was estimated using a mesh sensitivity analysis. In this analysis, the prediction of global behavior (load–CMOD curve) and local fracture characteristics such FPZ initiation stage and its size were evaluated for different element sizes in the central partition of the beam ranging from 2 to 0.1 mm. The elements size of 0.2 mm was found

to provide mesh independency in fracture behavior of the

## 3.3 Model Setup

The commercial general-purpose finite element package ABAOUS was used to simulate the crack propagation using the XFEM approach in the center-notched Barre granite specimen. Figure 4 shows the 2D model of the three-point bend test on barre granite specimen under plane stress condition. Due to the small specimen thickness (B = 25 mm) compared to other dimensions, the 2D model represents planar crack propagation through its entire thickness. The assumption is in agreement with other studies such as Rinehart et al. (2015) and Obara et al. (2020) that, based on a 3D model of three-point bending test, found crack propagation through entire specimen thickness with a straight crack front. The modeled specimen in the current study had the same nominal dimensions as the experiments with a 1 mm wide blunt notch with a semi-circular tip (Figs. 1b and 4), which resulted in a finite concentration of stresses around the notch tip. Simulation of a finite aperture notch was performed based on recommendations of various studies (e.g., Cusatis and Schauffert 2009; Luzio and Cusatis 2018) that have shown significant mesh dependency in predicting the FPZ characteristics for the case of crack propagation from sharp notches (stress singularity at the notch tip). These studies have suggested simulating the sharp notch as a finite aperture notch with a semi-circular tip. This has been shown to reduce mesh dependency provided a sufficiently refined

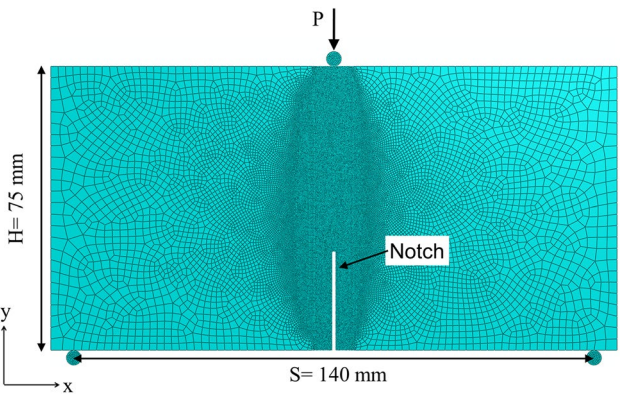


Fig. 4 Model geometry used for three-point bending test in ABAQUS

Barre granite specimen.

The material parameters of Barre granite are listed in Table 1. In the deterministic numerical model, the mean value of each parameter was used. The elastic parameters  $(E_t, \vartheta)$  were taken from the work of Goldsmith et al. (1976) to represent the elastic stiffness of Barre granite under tension. Goldsmith et al. (1976) based on uniaxial compression and uniaxial tensile strength tests on Barre granite found its

**Table 1** Input properties used in the deterministic model and random variable analysis

Parameter	Mean	Range	Coefficient of variation (COV)	Distribution	Truncation limit
Young's modulus $(E_t)$ (GPa)	28	19–80	20%	Lognormal	10–80
Tensile stress $(\sigma_t)$ (MPa)	14	5-20	20%	Lognormal	5–22
Critical inelastic crack opening $(w_{ne}^c)$ (µm)	32.5	21–58	27%	Lognormal	10–100
Poisson's ratio $(v)$	0.16	-	_	-	_



tensile elastic modulus ( $E_{\rm t}$ ) to be less than the compressive modulus ( $E_{\rm c}$ ) by a factor of 0.5. In the case of the tensile strength ( $\sigma_{\rm t}$ ), its most reported value based on the work of Goldsmith et al. (1976) and Ching et al. (2018) was used in the deterministic numerical model (Table 1). The average value of the critical inelastic crack opening ( $w_{\rm ne}^{\rm c}$ ) from four Barre granite specimens (BG-1, BG-2, BG-3, BG-4) was used in the deterministic numerical model (see mean in Table 1).

# 4 Random Variable Analysis

The presence of natural discontinuities (such as microdefect) typically lead to a scatter in fracture properties of Barre granite, such as tensile strength ( $\sigma_t$ ) and critical inelastic crack opening  $(w_{ne}^{c})$  as shown in Table 1. The uncertainties in the estimation of these parameters (used as input parameters in the numerical model) can lead to uncertainty in the determination of some fracture characteristics, such as the peak load and the FPZ size. To statistically characterize the overall fracture behavior, the input rock properties can be considered as random variables. Two widely used methods for this purpose are the Monte Carlo simulation (MCS) and point estimate methods (Harr 1989; Hong 1998). In this study, the MCS is adopted as it is simple and easy to implement. It involves repeated evaluation of the numerical model with randomly generated input parameters values from their respective probability distribution function (PDF). Since it is computationally expensive to directly conduct MCS on the numerical model, an alternative method such as explicit function (also known as the metamodel or the response surface) can be used as it acts as a surrogate to the numerical model. A linear polynomial augmented radial basis function (RBF) is adopted in this study since it can provide higher accuracy for both linear and nonlinear responses (Krishnamurthy 2003). This response surface methodology was employed in several other rock engineering problems (Wang et al. 2016; Pandit et al. 2019).

## 4.1 Input Property Distribution

In this study, only three input parameters, namely: (a) tensile elastic modulus ( $E_t$ ), (b) tensile strength ( $\sigma_t$ ) and (c) inelastic crack opening ( $w_{ne}^c$ ) are treated as uncorrelated random variables. The variation in tensile strength ( $\sigma_t$ ) of barre granite (see the range in Table 1) in the literature is typically smaller as compared to other igneous rocks (see rock database by Ching et al. 2018). Therefore, the lognormal distribution type with the Coefficient of Variation (COV) of 20% was used for tensile strength ( $\sigma_t$ ) in the current study, which is the lowest COV for typical granite rocks (Aladejare and Wang 2017). Additionally, tensile strength ( $\sigma_t$ ) is truncated

(see the limits in Table 1) to the range of values based on lab experiments available in the literature (Goldsmith et al. 1976; Miller 2008; Morgan et al. 2013; Ching et al. 2018; ASTM D3967). For a similar reason, the distribution of tensile elastic modulus  $(E_t)$ , is assumed to be lognormal with a COV of 20%. It is also truncated to ensure values from its distribution lie within the range of experimental data of Barre granite available in the literature (see the limits in Table 1). The inelastic crack opening displacement  $(w_{ne})$ varies from 21 to 58 µm based on DIC analysis of four lab experiments in the current study (Table 1). The COV of 27% was assumed for inelastic crack opening displacement  $(w_{ne})$  (Table 1), which lies in the range of observed variation (COV = 10-35%) of various quasi-brittle materials such as concrete and rocks (Bazant and Giraudon 2002; Yang et al. 2019). Additionally, the truncated limit of inelastic crack opening displacement  $(w_{ne})$  (see the limits in Table 1) was selected based on typically observed values for rocks (Zhang et al. 2018a, b; Lin et al. 2019b). All the input random variables are assumed independent lognormal distribution as it is widely adopted for most rock properties in the literature (Jiang et al. 2016; Pandit et al. 2019).

## 4.2 Response Surface

The numerical model is approximated using the RBF-based response surface augmented with a linear polynomial. Response surface construction involves solving numerical models on LH samples extracted from input space that serves as training data. The type of RBF adopted in this article is compact support function type II RBF developed by Wu (1995). For detailed methodology pertaining to construction and performance assessment of the augmented RBF, Pandit et al. (2019) can be referred.

## 5 Global Sensitivity Analysis

Since uncertainty in the input parameters leads to uncertainty in the output, it is necessary to study the contribution of each input parameter variability towards the output's variability. By identifying the sensitive input parameters, resources can be directed towards reducing the uncertainty in those parameters. Ranking of input parameters according to their magnitude of contribution towards the variability of output can be achieved by the global sensitivity analysis (GSA). GSA based on Sobol indices (Saltelli et al. 2008) quantifies the relative contribution of input parameters on the output variability. The individual contribution of each input parameter in output variability is denoted by first-order Sobol's indices ( $S_i$ ). The total effect ( $S_{T_i}$ ) includes interaction effects with other parameters in addition to the individual contribution. The estimate of  $S_i$  and  $S_{T_i}$  can be obtained by



MC-based approach, details of which are mentioned in the literature (Saltelli et al. 2008; Pandit and Babu 2020).

#### 6 Results

#### 6.1 FPZ Characterization

This section presents the characterization of the FPZ based on a consistent methodology developed by authors (for details, see Garg et al. 2020). This methodology used the concept of the LCZM to identify the transition between the three stages of FPZ evolution, namely: (a) the elastic deformation, (b) the FPZ initiation and its propagation, and (c) the macro-crack initiation that leads to unstable crack propagation. According to the LCZM, elastic opening displacement  $(w_e)$  represents the tip of the FPZ (i.e., the boundary between the elastic zone and the FPZ), while critical opening displacement  $(w_e)$  can be used to represents the tip of macro-crack (the boundary between the FPZ and macrocrack). In the adopted methodology, both elastic  $(w_e)$  and critical opening displacement  $(w_c)$  were estimated based on the evolution of crack opening displacement at the notch tip (CTOD) for Barre granite specimens (Garg et al. 2020). Figure 5a presents the contour of horizontal displacement at 75% of the peak during the post-peak stage of the test (i.e., 25% load drop from the peak was reached. Figure 5b shows the crack opening displacements (w) profiles at various loading stages. In order to quantify the CTOD in a consistent manner, two vertical lines at location  $x \pm 3$  mm from the notch plane (x=0) were selected to represent the virtual surfaces of the crack plane (Fig. 5a). The horizontal (normal) displacements were calculated between these two lines (Fig. 5a), also known as crack opening displacement (w), as shown in Fig. 5b.

Figure 6a shows the evolution of the CTOD with the normalized load-point displacement ( $\delta_{\mathrm{norm}}$ ) for four Barre granite specimens (BG-1, BG-2, BG-3, BG-4). The load-point displacement ( $\delta$ ) was normalized with respect to its value at the peak load stage ( $\delta_{\text{norm}} = \delta/\delta_{\text{peak}}$ ) for each specimen. In the adopted methodology, the elastic stage is characterized by the linear variation of CTOD with respect to normalized load-point displacement ( $\delta_{\mathrm{norm}}$ ) as observed in four Barre granite specimens (BG-1, BG-2, BG-3, BG-4) during initial

Pre-peak 81%

Post-peak 95%

Post-peak 80%

40

(b)

50

60

70

80

Fig. 5 a Contour of horizontal displacement (U) obtained using the DIC at 75% of the peak load in post-peak stage, and b Crack opening displacements (w) at various loading stages along with the method to identify the size of FPZ and TFZ using displacement approach

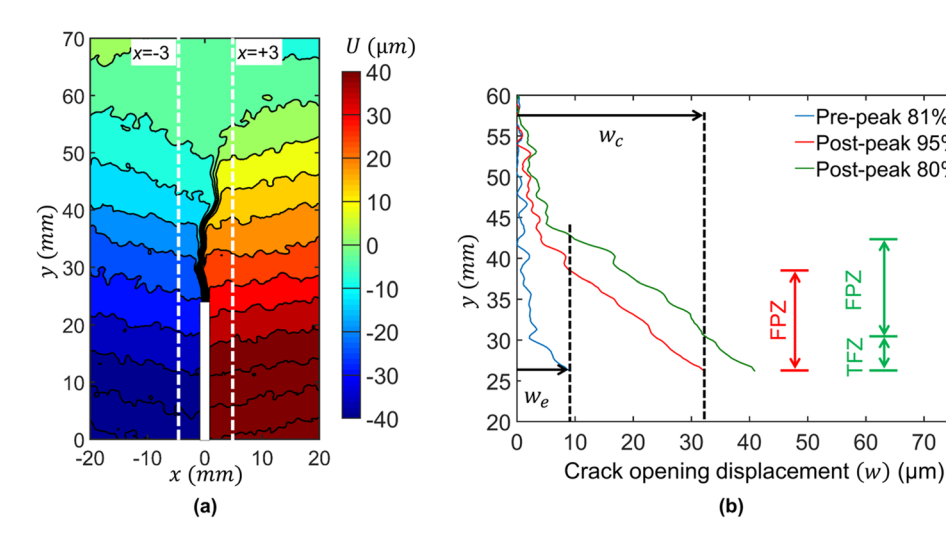
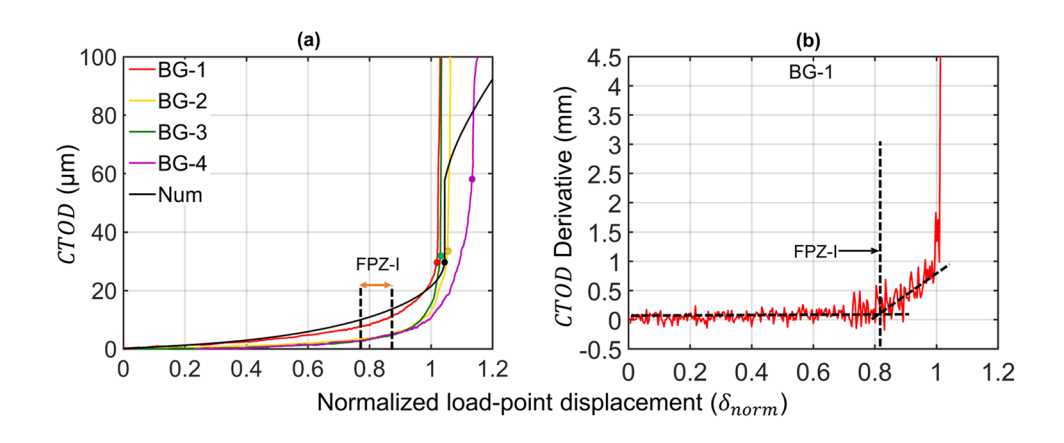


Fig. 6 Variation of a Crack tip opening displacement (CTOD) in numerical model and four Barre granite specimens (BG-1, BG-2, BG-3, BG-4), and b CTOD derivative for specimen BG-1 FPZ-I denotes FPZ initiation stage





loading stages (0–85% peak load in the pre-peak regime) (Fig. 6a). While, FPZ initiation from the notch tip is characterized by an accelerated rate of increase in CTOD resulting in its nonlinear variation with respect to normalized load-point displacement ( $\delta_{norm}$ ) starting from 80 to 85% of the peak load in the pre-peak stage (denoted by FPZ-I in Fig. 6a). The onset of non-linearity in the CTOD-normalized load-point displacement ( $\delta_{norm}$ ) curve is estimated as the point of the first significant change in the derivative of CTOD with respect to the normalized load-point displacement  $(\partial CTOD/\partial(\delta_{norm}))$  as shown in Fig. 6b for specimen BG-1. The macro-crack initiation, in the adopted methodology, is marked by the point of a rapid jump in CTOD with respect to a small change in the normalized load-point displacement ( $\delta_{norm}$ ) as shown by colored circles in all four specimens (Fig. 6a). The rapid jump in the CTOD can be attributed to the onset of the unstable crack propagation, which is a consequence of macro-crack (traction-free crack) initiation at the notch tip. For each specimen, the elastic opening displacement  $(w_e)$  is defined as the point of nonlinearity in CTOD vs. load-point displacement curve, while critical crack opening displacement  $(w_a)$  is estimated by the point of rapid jump in the CTOD. Table 2 presents the results of the four center notch specimens tested in this study. The FPZ length (l) is again estimated using the concept of the LCZM (Sect. 3.2) which defined the FPZ as the region with crack opening displacement (w) between elastic and critical opening displacements (i.e.,  $w_e < w < w_c$ ) as shown in Fig. 5b. It can be concluded that the evolution of CTOD provides a reliable method for the estimation of LCZM's parameters as it has shown consistent behavior for characterizing the three stages of the FPZ evolution in all Barre granite specimens (BG-1, BG-2, BG-3, BG-4) in accordance with finding by the previous study of authors (Garg et al. 2020).

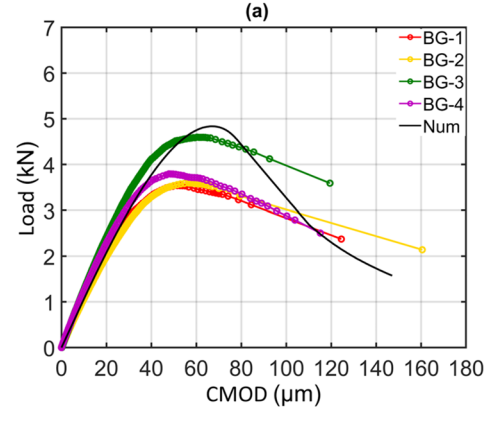
## **6.2 Deterministic Model**

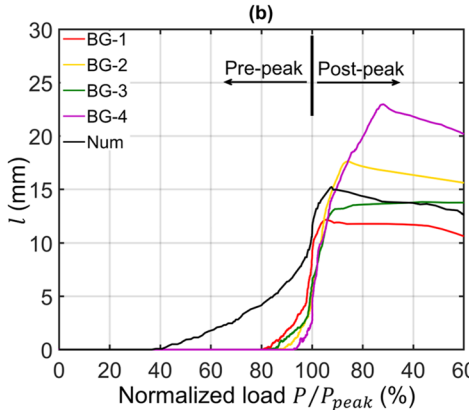
Figure 7a provides a comparison between the experimental and numerical results in terms of the applied vertical load as a function of the CMOD. It is clear from Fig. 7a that pre-peak responses of numerical model lie within the range of four experiments, indicating that the tensile elastic modulus ( $E_t$ ) of 28 GPa is an appropriate value to capture the elastic behavior of the Barre granite beam. However, the peak load stage was overestimated by the numerical model as both simulated peak load (4.83 kN) and peak CMOD (68  $\mu$ m) lie outside the range of values obtained from experiments (Fig. 7a). Similarly, the numerical model's post-peak response differed significantly with a steeper post-peak slope of the load–CMOD curve compared to experimental

Table 2 Comparison among output parameters obtained from different analyses

Output parameter	Mean	Standard deviation (COV)	95% confidence interval	Best fit distribution (parameters)	Deterministic numerical model	Experi- mental results
Peak load (kN)	4.8	0.74 (15%)	3.5–6.3	Normal (4.8, 0.74)	4.83	3.5–4.6
FPZ initiation load (%) (Prepeak regime)	38	5.07 (14%)	28.8–49.2	Lognormal (37.6, 5.07)	38	80–92
${\rm FPZ\ length}\ (L_{\rm FPZ})\ ({\rm mm})$	16.3	3.7 (23%)	10–24.5	Normal (16.3, 3.7)	15.4	12–23
Macro-crack initiation load (%) (Post-peak regime)	91.6	3.3 (3.6%)	84–96.8	Weibull (92.9, 34.17)	92	75–95

Fig. 7 Comparison between experimental and numerical results in terms of **a** applied load vs. crack mouth opening displacements (CMOD), and **b** FPZ length (*l*) vs. normalized applied load







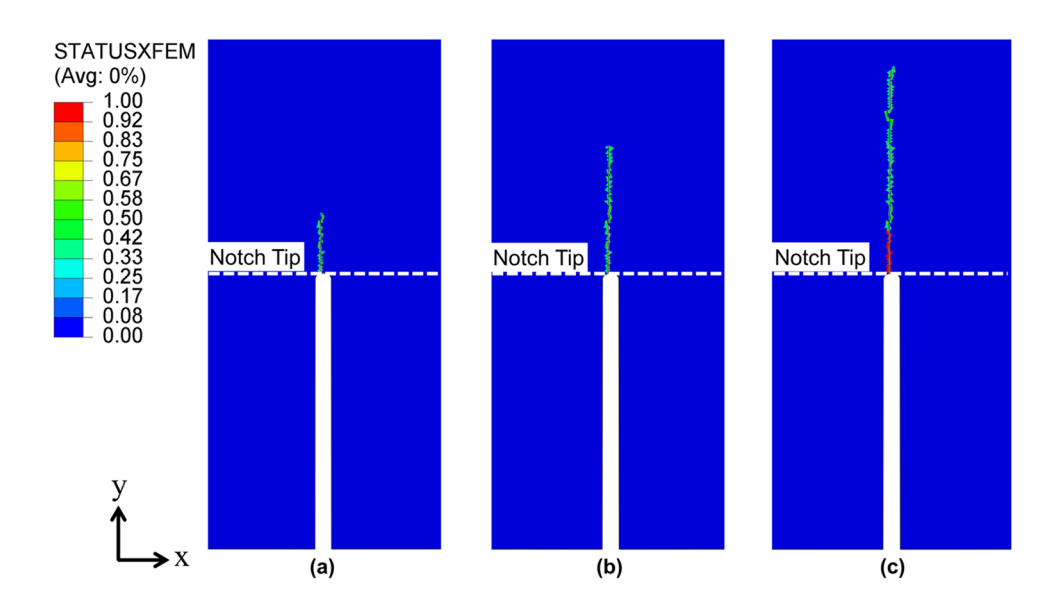
results. The difference in peak and post-peak response between numerical simulation and four experiments can be attributed to the material heterogeneity of granodiorite rocks such as Barre granite. Various studies (Nasseri et al. 2010; Wang and Hu 2017; Yu et al. 2018) have shown that the variability in different fracture characteristics such as the FPZ size and the tensile strength ( $\sigma_t$ ) of granite rocks typically depend on various factors such as microstructural anisotropy, grain size, initial notch length  $(a_0)$ , etc. For instance, Wang and Hu (2017), based on a three-point bending test on yellow granite, found that variability in peak load depends on initial notch length (relative to beam height) with a large fluctuation in peak load in the beam with smaller notches. Additionally, parameters of the LCZM were estimated based on average values of four Barre granite experimental data (Table 1), which were then directly used in the numerical model without any calibration. The fracture properties such as the critical crack opening displacement  $(w_c)$  (estimated from experiments in the current study) are highly dependent on the material behavior at a localized level and, thus, were strongly influenced by structural inhomogeneities such as micro-defects and the grain size. As a result, various CZM-based numerical studies (Song et al. 2006; Roesler et al. 2007; Im et al. 2014; Rinehart et al. 2015) typically used a calibration process where parameters of CZM such as critical crack opening displacement  $(w_c)$ , tensile strength  $(\sigma_t)$  and tensile elastic modulus  $(E_t)$  are iteratively changed until the entire global response (both pre-peak and post-peak regime) from the numerical model provides a good fit with experimental data.

Figure 7b shows the evolution of the FPZ length (l) with normalized load ( $P_{\text{norm}} = P/P_{\text{peak}}$ ) between four experiment results and the numerical simulation. The FPZ length (l) in four experiments was calculated using DIC analysis (Sect. 6.1). In the numerical model, the FPZ is represented

by elements undergoing progressive damage, denoted by the STATUSXFEM parameter (Fig. 8a–c). The parameter indicates the status of the element with the values between 0 and 1. A value of 1 (red color in Fig. 8a–c) denotes "completely fractured or traction-free crack," while value 0 indicates an elastic state. The elements with the value between 0 and 1 indicate the elements under softening and, thus, represent the FPZ. Figure 8a–c clearly shows the progression other FPZ at three different loading stages, namely (a) when 80% of the peak load, (b) when the peak load was applied, and (c) when 80% of the peak load was applied during the postpeak stage of the test (i.e., 20% load drop from the peak was reached).

Figure 7b clearly presents a consistent trend in the evolution of the FPZ length (l) between the numerical model and experiment results except for the FPZ initiation stage. The numerical model showed the FPZ initiation at an early stage (38% of peak load) compared to four experiments (80–92% of peak load). After initiation (Fig. 7b), both numerical model and four experimental tests showed a steady increase in the FPZ length (l) until the peak load (approximately 97–99% of peak load) followed by the rapid increase in post-peak regime to its maximum value around the macrocrack initiation stage (95-75% of peak load in the post-peak regime). The observation of the macro-crack initiation stage in the post-peak regime is consistent with various acoustic emission (AE)-based studies (Kao et al. 2011; Aggelis et al. 2013; Lin et al. 2019b) on rocks and other quasi-brittle materials. The FPZ at the macro-crack initiation stage is known as fully developed FPZ, and its length  $(L_{\text{FPZ}})$  (Fig. 3 in Sect. 3.2) is considered as a material property based on the LCZM. It can be inferred from Fig. 7b that, after reaching its maximum value in the post-peak regime, the FPZ length (1) remains nearly constant in the numerical model and four experiments (BG-1, BG-2, BG-3, BG-4) with the exception

Fig. 8 FPZ evolution in the numerical model at a 80% of the peak load (pre-peak stage), b peak load, and c post-peak stage when the load reached 80% of the peak load





of a slight decrease (1–3 mm). The observation agrees with the other studies (Lin and Labuz 2013; Lin et al. 2014; Zhang et al. 2018a, b) on various rocks such as Berea sandstone, Sichuan sandstone. Additionally, the length of fully developed FPZ ( $L_{\rm FPZ}$ ) obtained from the numerical model lie within the experimental range (Fig. 7b and Table 2), which is expected as its input parameters were based on average values of critical inelastic opening displacements ( $w_{\rm ne}^{\rm c}$ ) from four experiments (Table 1).

The early prediction of the FPZ initiation stage in the numerical model can be mainly attributed to the assumption of finite width FPZ as a thin interface by the LCZM. As a result, in the numerical model, the damage initiation is confined within the local element just above the notch tip and directly depends on the stress concentration within the element. In comparison, the FPZ initiation in the experiments is estimated based on the damage accumulation in the finite width micro-cracking zone, which leads to the overall inelastic behavior of material around the notch tip. In the current study, the evolution of CTOD was used to evaluate the material behavior over the notch tip, which is similar in the numerical model and four experiments (Fig. 6a in Sect. 6.1). Additionally, various AE-based studies (Zhang et al. 2018a, b; Lin et al. 2019b, 2020) have shown a small amount of material damage outside FPZ, suggesting that the assumption of linearly elastic behavior of material before FPZ initiation by the LCZM might not be entirely valid and thus can lead to errors in the prediction of FPZ initiation stage. The prediction of early FPZ initiation is consistent with the observation of various studies such as Moës and Belytschko (2002) and Ha et al. (2015), which have also found that the LCZM can predict the global response of quasi-brittle material such as concrete despite showing an early FPZ initiation stage. It can be concluded that LCZM estimated from standard tests can predict the FPZ evolution in Mode I fracture of Barre Granite with reasonable accuracy.

#### 6.3 Random Variable Model

In this study, 30 Latin Hypercube (LH) samples based on the study by Montgomery (2019) were extracted from input parameter distributions (Table 1), which were then used in numerical simulation of notched Barre granite specimens. The generated data from the numerical model were then used to construct an augmented RBF metamodel in MAT-LAB for each output parameter. The accuracy of the generated response surfaces was evaluated based on the error between the numerical models and augmented RBF obtained for additional 15 data sets (used as test samples). Moriasi et al. (2007) recommended Nash–Sutcliffe efficiency (NSE) as a quantitative index for performance assessment of the response surfaces. The NSE values of the response surface

Table 3 Accuracy of RBF-based response function for four output variables

Statistics	NSE value	Performance	
Peak load	0.998	Very good	
FPZ initiation load	0.8069	Very good	
FPZ length	0.9944	Very good	
Macro-crack initiation load	0.9969	Very good	

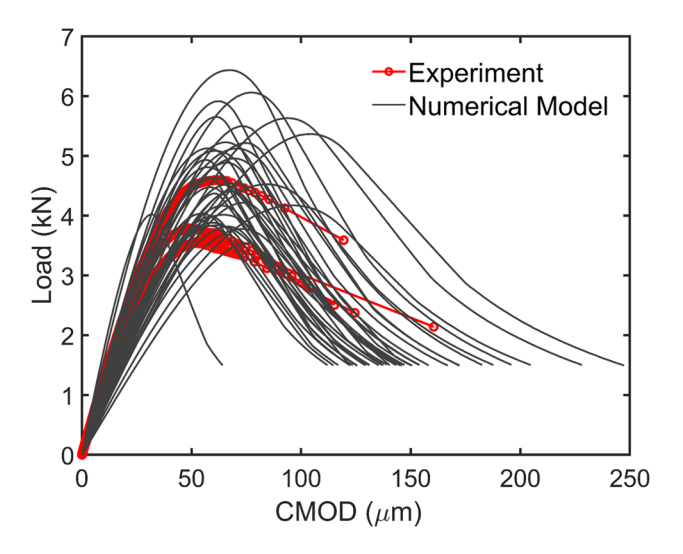


Fig. 9 Load versus CMOD curves predicted from Monte Carlo simulation along with experiments results of four Barre granite specimens

for each output (Table 3) suggest that the performance is *Very Good* (Moriasi et al. 2007), i.e., the numerical model approximation by augmented RBF response surface is *Very Good*. Figure 9 presents the Load–CMOD curves of 45 LH realizations (obtained from numerical simulation) against the experimental results. It is observed that the experimental curves lie within the range of the LH realized samples, i.e., the experimental data can be viewed as one of the realizations from the input probability distribution.

Uncertainty quantification of output variables is conducted by performing MCS on the response surface. Figure 10 presents the convergence of statistical moments of peak load for a different sequence of random numbers with increasing MCS. It can be seen that the variation in mean and standard deviation decreases with an increase in the number of realizations and become constant for 10<sup>5</sup>. realizations. Thus, 10<sup>5</sup> realizations are utilized for uncertainty quantification of outputs, and the results obtained are mentioned in Table 2. Table 4 presents the correlation coefficients between each output parameter obtained from MCS. It can be inferred from Table 2 that the mean of all four output parameters matches closely with values obtained from the deterministic numerical model, which again confirms the



**Fig. 10** Effect of the number of MCS on the mean and standard deviation of the peak load

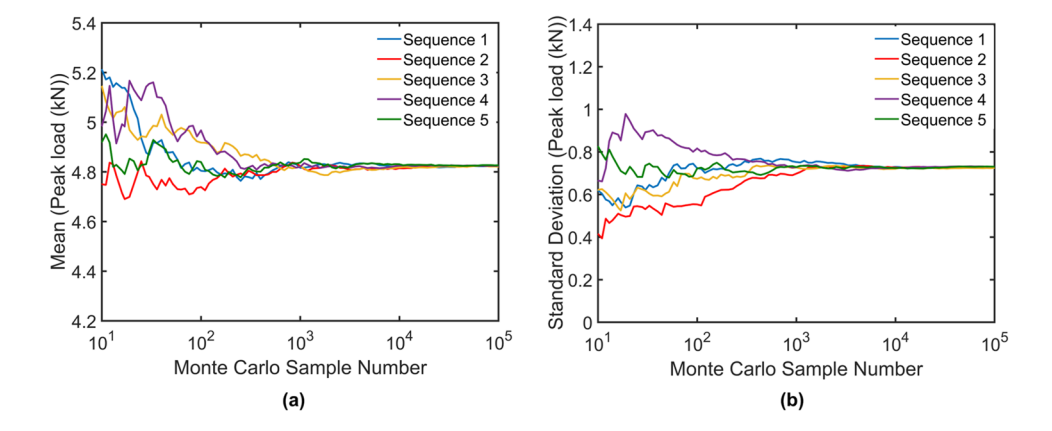


**Table 4** Correlation coefficient between each output parameters obtained from MCS

	Peak load	FPZ initiation load	FPZ length ( $L_{\text{FPZ}}$ )	Macro-crack initiation load
Peak load	1	- 0.1385	0.071	0.097
FPZ initiation load	-0.1385	1	- 0.8883	- 0.9206
FPZ length ( $L_{\text{FPZ}}$ )	0.071	-0.8883	1	0.9472
Macro-crack initiation load	0.097	- 0.9206	0.9472	1

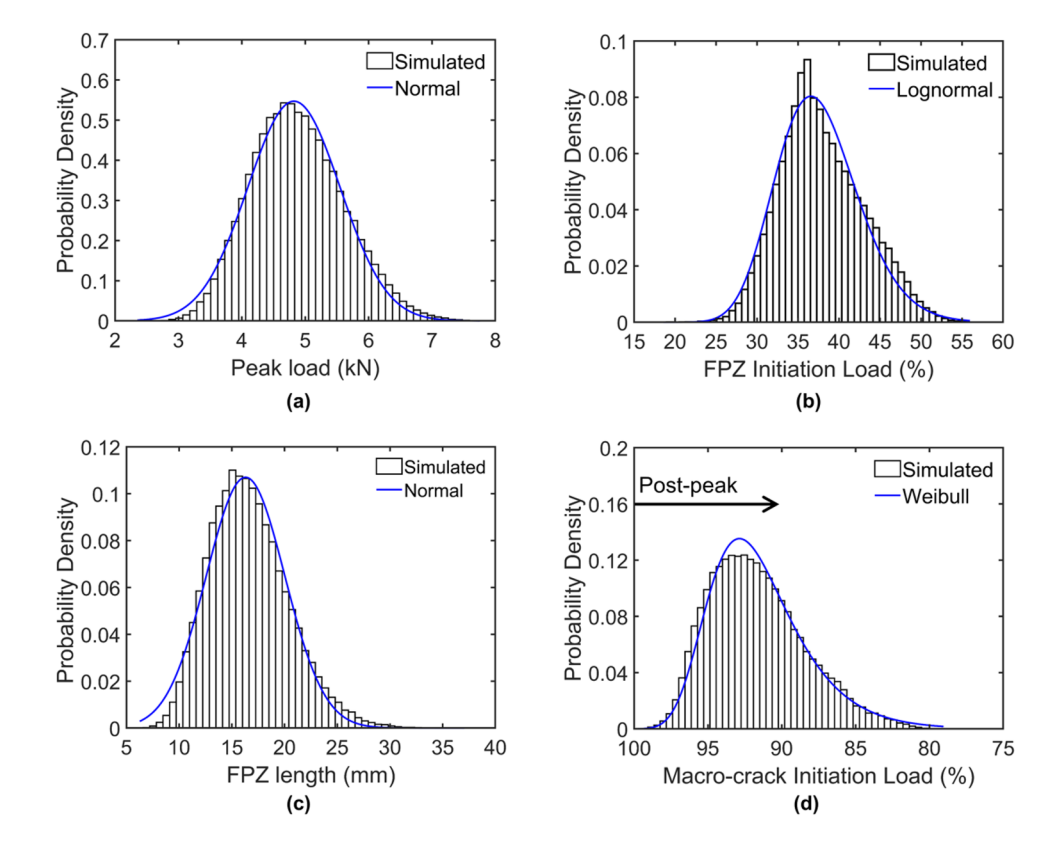
robustness of the response surface in the accurate approximation of the numerical model. Among all output parameters, the length of fully developed FPZ  $(L_{\text{FPZ}})$  has the maximum COV of 23%, which also lies within the range of the input parameters COVs (Tables 1 and 2). While the COV of other output parameters is smaller than the input COVs, with the macro-crack initiation load having the smallest COV of 3.6%. Additionally, the 95% confidence interval (CI) of all output parameters (except the FPZ initiation load) is similar to the range of experimental results (Table 2). The 95% CI of FPZ initiation load is significantly lower than the experimental range, which can be attributed to the numerical model's limitation as it underestimates the FPZ initiation stage (Sect. 6.2). Figure 11 shows distribution of each output parameters obtained from MCS on the response surface along with best-fit PDF. The statistics (mean and standard deviation) of best-fit PDFs for each output parameters is shown in Table 2.

A large variation of fully developed FPZ length ( $L_{\rm FPZ}$ ) in both MCS and experimental results can be attributed to it being a local property and, thus, strongly influenced by the material heterogeneity. Additionally, the 95% CI of fully developed FPZ ( $L_{\rm FPZ}$ ) from MCS is comparable to the notch length (0.38 <  $L_{\rm FPZ}/a_0$  < 0.94), indicating large scale yielding around notch tip and, thus, the assumption of LEFM (assume elastic stress distribution around crack tip) is not valid for the three-point bend specimens of Barre granite used in this study. Due to the significant size

of the FPZ around the notch tip, macro-crack initiation is most likely to occur during the post-peak stage of the test as shown in Fig. 11 with 95% CI of macro-crack initiation load around 84-97% of peak load in post-peak regime (Table 2). This can be further explained by a strong positive correlation between two parameters (Table 4), which indicates a higher energy dissipation inside the FPZ due to an increase in the FPZ length and thus delays macrocrack initiation. A similar correlation between the FPZ size and macro-crack initiation stage has been found by various studies (Hoagland et al. 1973; Parisio et al. 2019) in various rocks such as Salem limestone, Berea sandstone, and Adelaide black granite. Table 4 also shows that a strong negative correlation of FPZ initiation load with FPZ length  $(L_{\text{FPZ}})$  and macro-crack initiation load. It can be attributed to an increase in the tendency of material towards brittle fracture with an increase in the FPZ initiation load, which based on the LCZM directly depends on the tensile strength of the material  $(\sigma_t)$ . A higher FPZ initiation load (due to high tensile strength  $(\sigma_t)$ ) can lead to smaller FPZ length  $(L_{\text{FPZ}})$  and, thus, lower the energy dissipation across the fracture surface. As a result, higher energy can be available for macro-crack formation, which is more likely to occur at an early stage near the peak load stage. This observation is consistent with other studies such as Wang (2012) and Ha et al. (2015) that have found the FPZ length  $(L_{\rm FPZ})$  inversely proportional to tensile of the material  $(\sigma_t)$  that provides a measure of brittle fracture.



**Fig. 11** Histograms of each output parameter along best-fit PDFs



## 6.4 Global Sensitivity Analysis

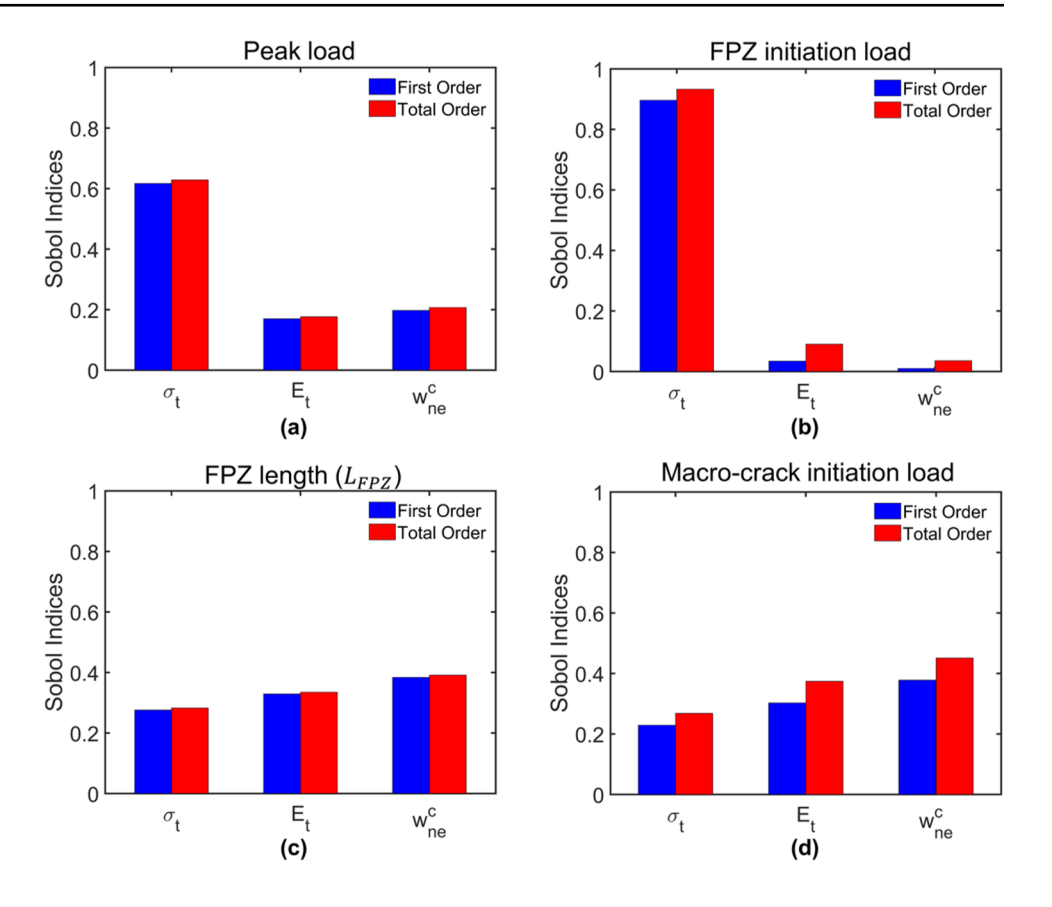
Both the first-order  $(S_i)$  and total-order  $(S_T)$  Sobol indices for output peak load clearly indicate that the variability of tensile strength  $(\sigma_t)$  has the highest contribution (60%) to the variability of peak load (Fig. 12a). The variabilities in the other two input parameters, i.e., critical inelastic crack opening  $(w_{ne}^c)$  and tensile elastic modulus  $(E_t)$  have a similar contribution of around 20% towards total variability of peak load (Fig. 12a). A high contribution of the tensile strength  $(\sigma_t)$  is expected as it is a critical parameter of the MPS criterion used for fracture initiation in the current study. A high tensile strength ( $\sigma_t$ ) can result in a beam with a large loadcarrying capacity, thereby increasing its peak/failure load. The recent studies by Wang and Hu (2017) and Zhang et al. (2018a, b) using this assumption developed an empirical formula for estimating tensile strength ( $\sigma_t$ ), fracture toughness  $(K_{Ic})$  based on Peak load measurements from three-point bending tests of various granite rocks. The critical inelastic crack opening  $(w_{ne}^{c})$  is proportional to energy dissipation along the unit length of the FPZ before macro-crack initiation. A higher critical inelastic crack opening  $(w_{ne}^{c})$  leads to higher resistance of material towards failure/fracture, thus consequently increases the peak load of the specimen. The high contribution of the tensile strength  $(\sigma_t)$  towards the variability of peak load is consistent with the observation by various studies (Song et al. 2006; Roesler et al. 2007)

that have found a larger influence of tensile strength  $(\sigma_t)$  than fracture energy  $(G_f)$ . (proportional to critical inelastic crack opening  $(w_{ne}^c)$ ) in different quasi-brittle materials such as concrete, asphalt mixture, etc. Similar to critical inelastic crack opening  $(w_{ne}^c)$ , tensile elastic modulus  $(E_t)$  also have a minor contribution towards variability of peak load. This can be attributed to the change in the specimen's elastic stiffness, which also leads to the change in FPZ characteristics, such as its size (discussed below), thereby changing the material resistance to failure. Additionally, the sum of first-order indices is 0.984 (less than 1, but close to 1), suggesting a negligible contribution from the higher-order interaction of input parameters (Fig. 12a).

The source of variability in the FPZ initiation load is predominantly due to the variability in tensile strength  $(\sigma_t)$  which accounts for over 90% of the total contribution (Fig. 12b), which can be attributed to the MPS criterion that predicts the FPZ initiation only based on material tensile strength  $(\sigma_t)$ . The small contribution of elastic modulus  $(E_t)$  (9%) can be attributed to minor changes in local stresses at the notch tip at a given load-point displacement  $(\delta)$  due to the change in elastic stiffness of the specimen (Fig. 12b). The LCZM use critical inelastic crack opening  $(w_{ne}^c)$  only for material softening and thus theoretically should have zero contribution toward variability of the FPZ initiation load. The small contribution (~3%) from inelastic crack opening  $(w_{ne}^c)$  can be considered as an error of the GSA.



Fig. 12 Sobol indices of the input parameters for each output parameter. Parameters include tensile strength  $(\sigma_t)$ , critical inelastic crack opening  $(w_{ne}^c)$  and elastic modulus  $(E_t)$ 



The FPZ length  $(L_{\rm FPZ})$  is most sensitive to critical inelastic crack opening  $(w_{ne}^c)$ , which accounts for 39% contribution towards its variability (Fig. 12c). This is expected as an increase in the critical inelastic crack opening  $(w_{ne}^{c})$ also increases the energy dissipation per unit length of the FPZ and, thus, facilitates a large FPZ size by increasing the material resistance towards fracture. This observation is consistent with the study by Ha et al. (2015) that have found fracture energy  $(G_f)$  (proportional to critical inelastic crack opening  $(w_{ne}^{c})$ ) directly proportional to the FPZ size. Similar to critical inelastic crack opening  $(w_{ne}^c)$ , tensile elastic modulus  $(E_t)$  also has a significant contribution towards FPZ length ( $L_{\text{FPZ}}$ ) (Fig. 12c), which typically results in a large FPZ size. This can be explained using the concept of characteristic length, which provide a theoretical estimate of the FPZ size (Bazant and Planas 1997) and is proportional to the tensile elastic modulus  $(E_t)$ . The tensile strength  $(\sigma_t)$  as mentioned earlier, increase the tendency of material towards brittle fracture; as a result, a material with high tensile strength ( $\sigma_t$ ) is more likely to have a small FPZ length  $(L_{\rm FPZ})$ . Therefore, tensile strength  $(\sigma_{\rm t})$  will likely to have a significant contribution (~28%) towards variability in the FPZ length ( $L_{\text{FPZ}}$ ) due to its negative correlation with the FPZ size (Fig. 12c). This observation is consistent with the various studies such as Wang (2012) and Ha et al. (2015) which found the FPZ size is inversely proportional to the square of the tensile strength ( $\sigma_t$ ) in the LCZM. For FPZ length, the higher-order interaction effects are to be negligible (Fig. 12c).

Similar to the FPZ length ( $L_{\rm FPZ}$ ) variabilities in all three input parameters had a significant contribution towards the variability in the macro-crack initiation load with the highest contribution (45%) of critical inelastic crack opening ( $w_{\rm ne}^c$ ) followed by the contribution of tensile elastic modulus ( $E_{\rm t}$ ) (~37%) and tensile strength ( $\sigma_{\rm t}$ ) (~27%) (Fig. 12d). This is expected as a high positive correlation exists in the FPZ length ( $L_{\rm FPZ}$ ) and macro-crack initiation load (Table 4).

## 7 Conclusion

While CZM is widely used to predict the overall fracture behavior of various quasi-brittle materials such as concrete, asphalt mixtures, its applicability in rocks has been limited due to large uncertainty in its parameters, which can be attributed to various factors. For instance, the inherent variability in tensile strength ( $\sigma_t$ ) and critical opening displacement ( $w_c$ ) can lead to variation in the global response of the rock specimens. In this study, an integrated approach was used to evaluate the LCZM's capability in predicting the fracture processes in notched Barre granite specimens by addressing three issues: (a)



consistent methodology for estimation of LCZM parameters, (b) variability in the input parameters of LCZM, and (c) most influential parameters of LCZM to minimize the uncertainty in overall rock fracture behavior. This approach was based on four steps: (a) experimental testing, (b) numerical simulation, (c) uncertainty quantification of material response, and (d) global sensitivity analysis. The main findings are summarized as follows:

- The evolution of CTOD obtained from DIC analysis can be used to characterize three stages of FPZ evolution in a consistent manner and, thus, provide a reliable method for estimating the parameters of the LCZM.
- 2. The LCZM implementation using the deterministic numerical model (XFEM-based simulation) was found inadequate in representing the variability in fracture behavior defined in terms of the peak load and the FPZ size observed in laboratory-scale Barre granite specimens. This variability can be attributed to variability in its input parameters such as tensile strength ( $\sigma_t$ ), critical inelastic crack opening ( $w_{ne}^c$ ) and elastic modulus ( $E_t$ ).
- 3. The variability of peak load (COV = 15%) obtained from MCS was consistent with variation typically found in three-point bend specimens of various rocks such as yellow granite and Harsin marble (Wang and Hu 2017; Aliha et al. 2018; Zhang et al. 2018a, b).
- 4. Despite variability in input parameters of the LCZM, a significant size of the FPZ around the notch tip was observed, indicating the large-scale yielding in the laboratory-scale Barre granite specimens under Mode I loading. As a result, macro-crack initiation is most likely to occur in the post-peak regime.
- 5. The results from GSA indicate that tensile strength ( $\sigma_t$ ) is the predominantly sensitive parameter towards variability in the global response of the Barre granite specimens. However, the variability in various fracture characteristics, such as the three stages of the FPZ evolution and its size, is sensitive to all three input parameters.

**Acknowledgements** Funding for this research was provided by the National Science Foundation under Award number 1644326. The authors are grateful for this support.

## References

- Abaqus Software (2016) Abaqus analysis user's guide. Dassault Systèmes Simulia Corp, Providence
- Aggelis DG, Verbruggen S, Tsangouri E et al (2013) Characterization of mechanical performance of concrete beams with external reinforcement by acoustic emission and digital image correlation. Constr Build Mater 47:1037–1045. https://doi.org/10.1016/j.conbuildmat.2013.06.005

- Aladejare AE, Wang Y (2017) Evaluation of rock property variability. Georisk Assess Manage Risk Eng Syst Geohazards 11:22–41. https://doi.org/10.1080/17499518.2016.1207784
- Alam SY, Saliba J, Loukili A (2014) Fracture examination in concrete through combined digital image correlation and acoustic emission techniques. Constr Build Mater 69:232–242. https://doi.org/10.1016/j.conbuildmat.2014.07.044
- Alam SY, Loukili A, Grondin F, Rozière E (2015) Use of the digital image correlation and acoustic emission technique to study the effect of structural size on cracking of reinforced concrete. Eng Fract Mech 143:17–31. https://doi.org/10.1016/j.engfracmech. 2015.06.038
- Aliha MRM, Ayatollahi MR (2014) Rock fracture toughness study using cracked chevron notched Brazilian disc specimen under pure modes I and II loading—a statistical approach. Theor Appl Fract Mech 69:17–25. https://doi.org/10.1016/j.tafmec. 2013.11.008
- Aliha MRM, Sistaninia M, Smith DJ et al (2012) Geometry effects and statistical analysis of mode I fracture in guiting limestone. Int J Rock Mech Mining Sci 51:128–135. https://doi.org/10.1016/j.ijrmms.2012.01.017
- Aliha MRM, Mahdavi E, Ayatollahi MR (2018) Statistical analysis of rock fracture toughness data obtained from different Chevron notched and straight cracked mode I specimens. Rock Mech Rock Eng 51:2095–2114. https://doi.org/10.1007/s00603-018-1454-9
- ASTM D3967-08 (2008) Standard test method for splitting tensile strength of intact rock core specimens. ASTM, West Conshohocken
- Backers T, Stanchits S, Dresen G (2005) Tensile fracture propagation and acoustic emission 895 activity in sandstone: the effect of loading rate. Int J Rock Mech Mining Sci 42:1094–1101. https://doi.org/10.1016/j.ijrmms.2005.05.011
- Baecher Gregory B, Christian John T (2003) Reliability and statistics in geotechnical engineering, 1st edn. Wiley, West Sussex
- Bazant ZP, Giraudon EB (2002) Statistical prediction of fracture parameters of concrete and implications for choice of testing standard. Cement Concr Res 32:529–556. https://doi.org/10.1016/S0008-8846(01)00723-2
- Bazant ZP, Planas J (1997) Fracture and size effect in concrete and other quasibrittle materials, 1st edn. CRC Press, Routledge
- Bazant ZP, Yu Q (2011) Size-effect testing of cohesive fracture parameters and nonuniqueness of work-of-fracture method. J Eng Mech 137:580–588. https://doi.org/10.1061/(ASCE)EM.1943-7889. 0000254
- Belytschko T, Black T (1999) Elastic crack growth in finite elements with minimal remeshing. Int J Numer Methods Eng 45:601–620. https://doi.org/10.1002/(SICI)1097-0207(19990620)45:5
- Borgonovo E (2007) A new uncertainty importance measure. Reliab Eng Syst Saf 92(6):771–784
- Bourcier M, Bornert M, Dimanov A et al (2013) Multiscale experimental investigation of crystal plasticity and grain boundary sliding in synthetic halite using digital image correlation. J Geophys Res Solid Earth 118:511–526. https://doi.org/10.1002/jgrb.50065
- Chen X, Deng X, Sutton MA, Zavattieri P (2014) An inverse analysis of cohesive zone model parameter values for ductile crack growth simulations. Int J Mech Sci 79:206–215. https://doi.org/10.1016/j.ijmecsci.2013.12.006
- Ching J, Li K-H, Phoon K-K, Weng M-C (2018) Generic transformation models for some intact rock properties. Can Geotech J 55:1702–1741. https://doi.org/10.1139/cgj-2017-0537
- Cusatis G, Schauffert EA (2009) Cohesive crack analysis of size effect. Eng Fract Mech 76:2163–2173. https://doi.org/10.1016/j.engfracmech.2009.06.008



Dai F, Xia K (2010) Loading rate dependence of tensile strength anisotropy of barre granite. Pure Appl Geophys 167:1419–1432. https://doi.org/10.1007/s00024-010-0103-3

- De Borst R (2003) Numerical aspects of cohesive-zone models. Eng Fract Mech 70:1743–1757. https://doi.org/10.1016/S0013-7944(03)00122-X
- Dual J, Schwarz T (2012) Acoustofluidics 3: Continuum mechanics for ultrasonic particle manipulation. Lab Chip 12:244–252. https:// doi.org/10.1039/C1LC20837C
- Eftekhari M, Baghbanan A, Hashemolhosseini H (2015) Extended finite element simulation of crack propagation in cracked Brazilian disc. J Mining Environ 6:95–102. https://doi.org/10.22044/jme.2015.365
- Elguedj T, Gravouil A, Maigre H (2009) An explicit dynamics extended finite element method. Part 1: Mass lumping for arbitrary enrichment functions. Comput Methods Appl Mech Eng 198:2297–2317. https://doi.org/10.1016/j.cma.2009.02.019
- Elices M, Guinea GV, Gómez J, Planas J (2002) The cohesive zone model: advantages, limitations and challenges. Eng Fract Mech 69:137–163. https://doi.org/10.1016/S0013-7944(01)00083-2
- Fakhimi A, Tarokh A (2013) Process zone and size effect in fracture testing of rock. Int J Rock Mech Mining Sci 60:95–102. https://doi.org/10.1016/j.ijrmms.2012.12.044
- Fan C, Jing XQ (2013) Numerical study of crack propagation path in three-point bending beam using extended finite element method. Appl Mech Mater 353–356:3615–3618.
- Garg P, Shirole D, Hedayat A, Griffiths DV (2019) Coupled ultrasonic and digital imaging of crack initiation and growth in prismatic Lyon sandstone rocks. In: Proceedings of 53rd U.S. rock mechanics/geomechanics symposium held in New York
- Garg P, Hedayat A, Griffiths DV Characterization of fracture process zone using surface deformation and strain field in brittle rocks. Rock Mech Rock Eng (**Under Review**)
- Ghamgosar M, Erarslan N (2016) Experimental and numerical studies on development of fracture process zone (FPZ) in rocks under cyclic and static loadings. Rock Mech Rock Eng 49:893–908. https://doi.org/10.1007/s00603-015-0793-z
- Giner E, Sukumar N, Tarancón JE, Fuenmayor FJ (2009) An Abaqus implementation of the extended finite element method. Eng Fract Mech 76:347–368. https://doi.org/10.1016/j.engfracmech.2008. 10.015
- Goldsmith W, Sackman JL, Ewerts C (1976) Static and dynamic fracture strength of Barre granite. Int J Rock Mech Mining Sci Geomech Abstr 13:303–309. https://doi.org/10.1016/0148-9062(76)91829-5
- Ha K, Baek H, Park K (2015) Convergence of fracture process zone size in cohesive zone modeling. Appl Math Model 39:5828– 5836. https://doi.org/10.1016/j.apm.2015.03.030
- Harr ME (1989) Probabilistic estimates for multivariate analyses. Appl Math Model 13:313–318. https://doi.org/10.1016/0307-904X(89) 90075-9
- Hedayat A, Walton G (2017) Laboratory determination of rock fracture shear stiffness using seismic wave propagation and digital image. Geotech Test J 40:92–106. https://doi.org/10.1520/GTJ20 160035
- Hedayat A, Pyrak-Nolte LJ, Bobet A (2014) Multi-modal monitoring of slip along frictional discontinuities. Rock Mech Rock Eng 47:1575–1587. https://doi.org/10.1007/s00603-014-0588-7
- Hillerborg A, Modéer M, Petersson P-E (1976) Analysis of crack formation and crack growth in concrete by means of fracture mechanics and finite elements. Cement Concr Res 6:773–781. https://doi.org/10.1016/0008-8846(76)90007-7
- Hoagland RG, Hahn GT, Rosenfield AR (1973) Influence of microstructure on fracture propagation in rock. Rock Mech 5:77–106. https://doi.org/10.1007/BF01240160

- Hong HP (1998) An efficient point estimate method for probabilistic analysis. Reliab Eng Syst Saf 59:261–267. https://doi.org/10. 1016/S0951-8320(97)00071-9
- Im S, Ban H, Kim Y-R (2014) Characterization of mode-I and mode-II fracture properties of fine aggregate matrix using a semicircular specimen geometry. Constr Build Mater 52:413–421. https://doi.org/10.1016/j.conbuildmat.2013.11.055
- Iqbal MJ, Mohanty B (2006) Experimental calibration of ISRM suggested fracture toughness measurement techniques in selected brittle rocks. Rock Mech Rock Eng 40:453. https://doi.org/10.1007/s00603-006-0107-6
- Ji WW, Pan PZ, Lin Q et al (2016) Do disk-type specimens generate a mode II fracture without confinement? Int J Rock Mech Min Sci 87:48–54. https://doi.org/10.1016/j.ijrmms.2016.05.010
- Jiang Q, Zhong S, Cui J et al (2016) Statistical characterization of the mechanical parameters of intact rock under triaxial compression: an experimental proof of the jinping marble. Rock Mech Rock Eng 49:4631–4646. https://doi.org/10.1007/ s00603-016-1054-5
- Kao C-S, Carvalho FCS, Labuz JF (2011) Micromechanisms of fracture from acoustic emission. Int J Rock Mech Min Sci 48:666–673. https://doi.org/10.1016/j.ijrmms.2011.04.001
- Karihaloo BL, Xiao QZ (2003) Modelling of stationary and growing cracks in FE framework without remeshing: a state-of-the-art review. Comput Struct 81:119–129. https://doi.org/10.1016/S0045-7949(02)00431-5
- Khoei AR (2014) Extended finite element method: theory and applications, 1st edn. Wiley, West Sussex
- Khoei AR, Mohammadnejad T (2011) Numerical modeling of multiphase fluid flow in deforming porous media: a comparison between two- and three-phase models for seismic analysis of earth and rockfill dams. Comput Geotech 38:142–166. https://doi.org/10.1016/j.compgeo.2010.10.010
- Khoramishad H, Akbardoost J, Ayatollahi MR (2013) Size effects on parameters of cohesive zone model in mode I fracture of limestone. Int J Damage Mech 23:588–605. https://doi.org/10.1177/ 1056789513504319
- Krishnamurthy T (2003) Response surface approximation with augmented and compactly supported radial basis functions. In: 44th AIAA/ASME/ASCE/AHS/ASC structures, structural dynamics, and materials conference. American Institute of Aeronautics and Astronautics
- Labuz JF, Shah SP, Dowding CH (1987) The fracture process zone in granite: evidence and effect. Int J Rock Mech Min Sci Geomech Abstr 24:235–246. https://doi.org/10.1016/0148-9062(87) 90178-1
- Le J-L, Manning J, Labuz JF (2014) Scaling of fatigue crack growth in rock. Int J Rock Mech Min Sciences 72:71–79. https://doi.org/10.1016/j.ijrmms.2014.08.015
- Lin Q, Labuz JF (2013) Fracture of sandstone characterized by digital image correlation. Int J Rock Mech Min Sci 60:235–245. https:// doi.org/10.1016/j.ijrmms.2012.12.043
- Lin Q, Fakhimi A, Haggerty M, Labuz JF (2009) Initiation of tensile and mixed-mode fracture in 990 sandstone. Int J Rock Mech Min Sci 46(489–497):991. https://doi.org/10.1016/j.ijrmms.2008.10.
- Lin Q, Yuan H, Biolzi L, Labuz JF (2014) Opening and mixed mode fracture processes in a quasi-brittle material via digital imaging. Eng Fract Mech 131:176–193. https://doi.org/10.1016/j.engfracmech.2014.07.028
- Lin Q, Wan B, Wang S et al (2019a) Visual detection of a cohesionless crack in rock under three-point bending. Eng Fract Mech 211:17–31. https://doi.org/10.1016/j.engfracmech.2019.02.009
- Lin Q, Wan B, Wang Y et al (2019b) Unifying acoustic emission and digital imaging observations of quasi-brittle fracture.



- Theor Appl Fract Mech. https://doi.org/10.1016/j.tafmec.2019. 102301
- Lin Q, Wang S, Pan PZ et al (2020) Imaging opening-mode fracture in sandstone under three-point bending: a direct identification of the fracture process zone and traction-free crack based on cohesive zone model. Int J Rock Mech Min Sci 136:104516. https://doi.org/10.1016/j.ijrmms.2020.104516
- Lu Y, Li W, Wang L et al (2019) In-situ microscale visualization experiments on microcracking and microdeformation behaviour around a pre-crack tip in a three-point bending sandstone. Int J Rock Mech Min Sci 114:175–185. https://doi.org/10.1016/j.ijrmms.2019.01.002
- Luzio GD, Cusatis G (2018) Cohesive crack analysis of size effect for samples with blunt notches and generalized size effect curve for quasi-brittle materials. Eng Fract Mech 204:15–28. https://doi.org/10.1016/j.engfracmech.2018.09.003
- Miao S, Pan PZ, Yu P et al (2020) Fracture analysis of Beishan granite after high-temperature treatment using digital image correlation. Eng Fract Mech. https://doi.org/10.1016/j.engfracmech. 2019.106847
- Miller JT (2008) Crack coalescence in granite. MSc Thesis, Massachusetts Institute of Technology
- Moës N, Belytschko T (2002) Extended finite element method for cohesive crack growth. Eng Fract Mech 69:813–833. https://doi.org/10.1016/S0013-7944(01)00128-X
- Montgomery DC (2019) Design and analysis of experiments 8th Edition, 10th edn. Wiley, New York
- Moradian Z, Einstein HH, Ballivy G (2016) Detection of cracking levels in brittle rocks by parametric analysis of the acoustic emission signals. Rock Mech Rock Eng 49:785–800. https://doi.org/10.1007/s00603-015-0775-1
- Morgan SP, Johnson CA, Einstein HH (2013) Cracking processes in Barre granite: fracture process zones and crack coalescence. Int J Fract 180:177–204. https://doi.org/10.1007/s10704-013-9810-y
- Moriasi D, Arnold J, Liew M et al (2007) Model evaluation guidelines for systematic quantification of accuracy in watershed simulations. Trans ASABE 50:885–900
- Nasseri MHB, Grasselli G, Mohanty B (2010) Fracture toughness and fracture roughness in anisotropic granitic rocks. Rock Mech Rock Eng 43:403–415. https://doi.org/10.1007/s00603-009-0071-z
- Oakley JE, O'Hagan A (2004) Probabilistic sensitivity analysis of complex models: a Bayesian approach. J R Stat Soc Ser B (stat Methodol) 66(3):751–769
- Obara Y, Nakamura K, Yoshioka S et al (2020) Crack front geometry and stress intensity factor of semi-circular bend specimens with straight through and chevron notches. Rock Mech Rock Eng 53:723–738. https://doi.org/10.1007/s00603-019-01930-5
- Oh J-C, Kim H-G (2013) Inverse estimation of cohesive zone laws from experimentally measured displacements for the quasi-static mode I fracture of PMMA. Eng Fract Mech 99:118–131. https://doi.org/10.1016/j.engfracmech.2012.11.002
- Pan B, Asundi A, Xie H, Gao J (2009a) Digital image correlation using iterative least squares and pointwise least squares for displacement field and strain field measurements. Opt Lasers Eng 47:865–874. https://doi.org/10.1016/j.optlaseng.2008.10.014
- Pan B, Qian K, Xie H, Asundi A (2009b) Two-dimensional digital image correlation for in-plane displacement and strain measurement: a review. Meas Sci Technol 20:062001. https://doi.org/10. 1088/0957-0233/20/6/062001
- Pandit B, Babu GL (2020) Global sensitivity analysis of rockmass and support design parameters in tunnel-support system. In: 54th US rock mechanics/geomechanics symposium. American Rock Mechanics Association
- Pandit B, Tiwari G, Latha GM, Babu GLS (2019) Probabilistic characterization of rock mass from limited laboratory tests and field data: associated reliability analysis and its interpretation.

- Rock Mech Rock Eng 52:2985-3001. https://doi.org/10.1007/s00603-019-01780-1
- Parisio F, Tarokh A, Makhnenko R et al (2019) Experimental characterization and numerical modelling of fracture processes in granite. Int J Solids Struct 163:102–116. https://doi.org/10.1016/j.ijsolstr.2018.12.019
- Patel S, Martin CD (2018) Evaluation of tensile young's modulus and Poisson's ratio of a bi-modular rock from the displacement measurements in a Brazilian test. Rock Mech Rock Eng 51:361–373. https://doi.org/10.1007/s00603-017-1345-5
- Planas J, Elices M, Guinea GV et al (2003) Generalizations and specializations of cohesive crack models. Eng Fract Mech 70:1759–1776. https://doi.org/10.1016/S0013-7944(03)00123-1
- Rinehart AJ, Bishop JE, Dewers T (2015) Fracture propagation in Indiana Limestone interpreted via linear softening cohesive fracture model. J Geophys Res Solid Earth 120:2292–2308. https://doi.org/10.1002/2014JB011624
- Roesler J, Paulino GH, Park K, Gaedicke C (2007) Concrete fracture prediction using bilinear softening. Cement Concr Compos 29:300–312. https://doi.org/10.1016/j.cemconcomp.2006.12.002
- Saadat M, Taheri A (2019) Modelling micro-cracking behaviour of pre-cracked granite using grain-based distinct element model. Rock Mech Rock Eng 52:4669–4692. https://doi.org/10.1007/ s00603-019-01862-0
- Saltelli A, Ratto M, Andres T et al (2008) Global sensitivity analysis: the Primer, 1st edn. Wiley, West Sussex
- Schreier H, Orteu J-J, Sutton MA (2009) Image Correlation for Shape. Motion and Deformation Measurements, Springer, US, Boston
- Sharafisafa M, Nazem M (2014) Application of the distinct element method and the extended finite element method in modelling cracks and coalescence in brittle materials. Comput Mater Sci 91:102–121. https://doi.org/10.1016/j.commatsci.2014.04.006
- Sharpe WN (2008) Springer handbook of experimental solid mechanics. William N. Springer US, Boston
- Shet C, Chandra N (2004) Effect of the shape of T–δ cohesive zone curves on the fracture response. Mech Adv Mater Struct 11:249–275. https://doi.org/10.1080/15376490490427207
- Shirole D, Walton G, Hedayat A (2020) Experimental investigation of multi-scale strain-field heterogeneity in rocks. Int J Rock Mech Min Sci. https://doi.org/10.1016/j.ijrmms.2020.104212
- Soares JB, de Freitas FAC, Allen DH (2003) Considering material heterogeneity in crack modeling of asphaltic mixtures. Transp Res Rec 1832:113–120. https://doi.org/10.3141/1832-14
- Sobol IM (1993) Sensitivity estimates for nonlinear mathematical models. Math Mod Comput Exp 1:407–414
- Song SH, Paulino GH, Buttlar WG (2006) Simulation of crack propagation in asphalt concrete using an intrinsic cohesive zone model. J Eng Mech 132:1215–1223. https://doi.org/10.1061/(ASCE) 0733-9399(2006)132:11(1215)
- Sutton MA, Yan JH, Deng X et al (2007) Three-dimensional digital image correlation to quantify deformation and crack-opening displacement in ductile aluminum under mixed-mode I/III loading. Opt Eng 46:1–17. https://doi.org/10.1117/1.2741279
- Wang JT (2012) Investigating some technical issues on cohesive zone modeling of fracture. J Eng Mater Technol. https://doi.org/10. 1115/1.4007605
- Wang Y, Hu X (2017) Determination of tensile strength and fracture toughness of granite using notched three-point-bend samples. Rock Mech Rock Eng 50:17–28. https://doi.org/10.1007/s00603-016-1098-6
- Wang Q, Fang H, Shen L (2016) Reliability analysis of tunnels using a metamodeling technique based on augmented radial basis functions. Tunn Undergr Space Technol 56:45–53. https://doi.org/10. 1016/j.tust.2016.02.007
- Wu Z (1995) Compactly supported positive definite radial functions. Adv Comput Math 4:283. https://doi.org/10.1007/BF03177517



Xie Y, Cao P, Jin J, Wang M (2017) Mixed mode fracture analysis of semi-circular bend (SCB) specimen: a numerical study based on extended finite element method. Comput Geotech 82:157–172. https://doi.org/10.1016/j.compgeo.2016.10.012

- Xing Y, Zhang G, Wan B, Zhao H (2019) Subcritical fracturing of sandstone characterized by the acoustic emission energy. Rock Mech Rock Eng 52:2459–2469. https://doi.org/10.1007/ s00603-018-1724-6
- Xu Y, Li X, Wang X, Liang L (2014) Inverse parameter identification of cohesive zone model for simulating mixed-mode crack propagation. Int J Solids Struct 51:2400–2410. https://doi.org/10.1016/j.ijsolstr.2014.03.008
- Yang J, Lian H, Liang W et al (2019) Model I cohesive zone models of different rank coals. Int J Rock Mech Min Sci 115:145–156. https://doi.org/10.1016/j.ijrmms.2019.01.001
- Yao Y (2012) Linear elastic and cohesive fracture analysis to model hydraulic fracture in brittle and ductile rocks. Rock Mech Rock Eng 45:375–387. https://doi.org/10.1007/s00603-011-0211-0
- Yu M, Wei C, Niu L et al (2018) Calculation for tensile strength and fracture toughness of granite with three kinds of grain sizes using three-point-bending test. PLoS ONE. https://doi.org/10.1371/journal.pone.0180880
- Zhang C, Hu X, Wu Z, Li Q (2018a) Influence of grain size on granite strength and toughness with reliability specified by normal

- distribution. Theor Appl Fract Mech 96:534–544. https://doi.org/10.1016/j.tafmec.2018.07.001
- Zhang G, Xing Y, Wang L (2018b) Comprehensive sandstone fracturing characterization: integration of fiber Bragg grating, digital imaging correlation and acoustic emission measurements. Eng Geol 246:45–56. https://doi.org/10.1016/j.enggeo.2018.09.016
- Zhou X-P, Chen J-W, Berto F (2020) XFEM based node scheme for the frictional contact crack problem. Comput Struct 231:106221. https://doi.org/10.1016/j.compstruc.2020.106221
- Zhuang X, Chun J, Zhu H (2014) A comparative study on unfilled and filled crack propagation for rock-like brittle material. Theor Appl Fract Mech 72:110–120. https://doi.org/10.1016/j.tafmec. 2014.04.004
- Zi G, Belytschko T (2003) New crack-tip elements for XFEM and applications to cohesive cracks. Int J Numer Methods Eng 57:2221–2240. https://doi.org/10.1002/nme.849

**Publisher's Note** Springer Nature remains neutral with regard to jurisdictional claims in published maps and institutional affiliations.

